Greek mountain snow cover halved in past four decades due to regional warming

Konstantis Alexopoulos[1,2,3], Ian C. Willis[1], Hamish D. Pritchard[4], Giorgos Kyros[2,3], Vassiliki Kotroni[2], Konstantinos Lagouvardos[2]

[1]Scott Polar Research Institute, University of Cambridge, Cambridge, CB2 1ER, United Kingdom
[2]Institute of Environmental Research and Sustainable Development, National Observatory of Athens, Athens, 15236, Greece
[3]Hellenic Mountain Observatory, Piraeus, 18531, Greece
[4]British Antarctic Survey, Cambridge, CB3 0ET, United Kingdom

Correspondence to: Konstantis Alexopoulos (konstantis.alexopoulos@gmail.com)

Abstract. Snowpacks in mountain regions with Mediterranean climates are exceptionally sensitive to climate warming. However, these marginal snowpacks are sparsely monitored, limiting our understanding of recent snow losses and constraining our ability to anticipate and manage future changes in mountain water supply. Here we present snowMapper v1.0, an iteratively-solved, physics-informed machine learning model for reconstructing daily snow cover at high spatial resolution using satellite imagery and gridded climate products. snowMapper is fully configurable and features dedicated modules for masking, preprocessing, snow binarization, snow reconstruction, spatiotemporal aggregation, and validation. It performs with exceptionally high skill. Using snowMapper, we generate a monthly snow-cover climatology for ten of Greece's highest mountain massifs for the period 1984-2025. Our results reveal a rapid and widespread decline in snow cover area (SCA), amounting to a ~ 58 % reduction relative to the 1984-2025 mean. We identify sustained warming throughout the snow season as the primary driver of this decline. Precipitation changes correlate with SCA only in early and mid-winter, underscoring the dual role of air temperature in controlling both accumulation (via snowfall fraction) and ablation processes. The North Atlantic Oscillation exerts only a modest influence on mid-winter SCA, and primarily when acting in conjunction with the Arctic Oscillation, representing a stark contrast to patterns observed in western Mediterranean mountain ranges. Finally, the absence of a strong relationship between SCA and the Atlantic Multidecadal Oscillation reinforces the conclusion that the observed trends lie outside the bounds of natural climate variability.

1 Introduction

Mountains play a vital role in regulating the water supply to ecosystems and populations downstream (Viviroli et al., 2007). In the Mediterranean region, precipitation is strongly seasonal, peaking in autumn and winter, with a large fraction of it falling at higher elevations as snow (Fayad et al., 2017). The seasonal lag between snow accumulation and its subsequent meltwater release later in the hydrological year helps to mitigate summer water deficits, when demand is highest and precipitation is lowest (Avanzi et al., 2024; García-Ruiz et al., 2011; López-Moreno et al., 2024; Loukas et al., 2007). This delayed runoff is especially critical in basins with limited artificial storage capacity - common in the region - where a significant fraction of winter precipitation would otherwise be lost as runoff to the sea, reducing its availability for ecosystems and for domestic, agricultural, and industrial use (Barnett et al., 2005; Shea et al., 2021). Moreover, the Mediterranean mountain ranges outside of the Alps lack major glaciers, which act as natural hydrological buffers during years of meteorological drought (Pritchard, 2019). This absence heightens dependence on climatically marginal snowpacks, which are inherently vulnerable to warming owing to their predominantly isothermal state (López-Moreno et al., 2024, 2025).

Since the early 21st century, the Mediterranean region has been recognised as a climate change "hotspot," experiencing some of the fastest rates of environmental change globally (Giorgi, 2006). Although debate continues over whether regional precipitation trends reflect anthropogenic forcing or natural variability (Trancoso et al., 2024; Vicente-Serrano et al., 2025), there are robust signals of rising temperatures, which are consistently linked to a declining snowfall fraction and earlier snowmelt across the region's mountain ranges (Akyurek et al., 2023; Alonso-González et al., 2020; Capozzi et al., 2025; Choler et al., 2025; Fayad et al., 2017; Gottlieb and Mankin, 2024; Li et al., 2025; López-Moreno et al., 2017, 2025; Masloumidis et al., 2025; Notarnicola, 2020, 2024b). These regional changes are further amplified by the global phenomenon of elevation-dependent warming, which enhances temperature increases in mountain environments and alters associated precipitation regimes (Abbas et al., 2024; Pepin et al., 2015, 2022).

Although marginal snowpacks are crucial to ecosystems and society, and are highly sensitive to climate change, research into their climatology remains limited to a few well-studied ranges, such as the European Alps and the Pyrenees, with little to no information available for the other ranges (Fayad et al., 2017; López-Moreno et al., 2024). In the Balkan Peninsula, extreme minimum temperatures exhibit a positive latitudinal gradient, and the frequency of winter cold spells declines towards the end of the 1961-2019 period (Tringa et al., 2022). Large negative trends in snowfall have also been identified across the Peninsula's mountain regions between 1979-2018 (Faranda, 2020).

In Greece, analyses of snow cover days between 1991-2020, indicate an initial increase followed by rapid declines of up to -1.5 days yr^{-1}, with reductions becoming more frequent and severe in the latter half of the study period (Masloumidis et al., 2025). Similar patterns are reported for snow depth and snow water equivalent in two lowland catchments in northern Greece, based on the Global Land Data Assimilation System Noah Land Surface Model L4 V2.0, at a 0.25° resolution (Voudouri et al., 2023). According to Masloumidis et al. (2025), the strongest and statistically significant trends are concentrated in winter, particularly in the mountains of northwestern Greece. However, these findings may be constrained by the coarse spatial resolution of the underlying reanalysis products. Although CERRA-Land provides relatively high resolution for such datasets (~5.5 km), its ability to resolve snow processes at finer spatial scales (such as small mountain massifs) or during transitional periods (autumn and spring), remains limited (Monteiro and Morin, 2023). The inclusion of September and October in the definition of autumn snow cover by Masloumidis et al. (2025) may have also obscured early snow season trends, given that snow onset in the Greek mountains typically occurs in November. Consequently, analyses based on higher resolution datasets may reveal stronger and more spatiotemporally heterogenous trends.

Indeed, a MODIS-based snow cover phenology dataset at 500 m resolution for the 2000-2023 period show declines in snow cover duration of up to -4.1 days yr^{-1} across the Greek mountains (Notarnicola, 2024a), nearly three times the maximum rate reported in courser-resolution analyses (Masloumidis et al., 2025). While these high-resolution data offer valuable insight into sub-kilometre-scale snow cover variability, expanding the temporal coverage to earlier decades would further improve understanding of long-term changes and their relationship to ongoing climate change.

Given the substantial spatial and temporal limitations of in situ snow observations, satellite remote sensing has long provided a valuable alternative for investigating mountain snow hydrology (Fayad et al., 2017; Gascoin et al., 2024). However, gaps in satellite records—due to persistent cloud cover and, low revisit frequency, especially in the earlier missions—limit the utility of these datasets in their original form. To overcome these limitations, researchers have developed a variety of gap-filling and data aggregation methods. These include decision tree-based approaches leveraging snowline altitude for detection and interpolation (Gascoin et al., 2019; Koehler et al., 2022); yearly aggregation techniques that normalise observations across multiple decades (Moazzam et al., 2022); and more advanced frameworks that combine snowline-based gap-filling with monthly aggregation (Poussin et al., 2024). Spatial and temporal filtering methods have also been employed, using neighbouring grid cells in space and time, respectively, to reconstruct missing binary snow-cover data (Barrou Dumont et al., 2025; Gafurov and Bárdossy, 2009; Gascoin et al., 2015, 2022; Notarnicola, 2020; Parajka and Blöschl, 2008). Another approach has employed a machine learning classifier trained on a combination of MODIS and reanalysis-derived spatial aggregates of fractional snow cover, using the latter to extend the MODIS record into the past (Gascoin et al., 2022). More recently, a climatology-based method was introduced for gap-filling by linking preceding meteorological conditions to snow cover patterns and identifying analogous states through a k-nearest neighbour algorithm (Zakeri and Mariethoz, 2024).

Despite their effectiveness in specific contexts, these techniques entail notable trade-offs. First, spatial filters require a sufficient number of same-day observations (pixels), restricting their use to periods with adequate imagery and forcing a choice between datasets: the high spatial resolution but low revisit frequency of, e.g., Landsat or Sentinel-2, versus the higher frequency but coarser resolution of, e.g., MODIS. Second, temporal filters can reliably bridge data gaps of only 5–10 days, making them unsuitable for much of the early Landsat record, where gaps often far exceed this range due to limited satellite coverage, persistent cloud contamination, and the Scan Line Corrector (SLC) failure of Landsat 7's ETM+ sensor. Third, temporal aggregation methods applied on unevenly captured imagery, even when supplemented with gap-filling steps, inherently sacrifice day-to-day variability and risk introducing substantial bias, for example when a single early- or late-month observation is used to represent an entire month's snow conditions.

Physics-informed machine learning (PIML) integrates data-driven machine learning algorithms with physical constraints embedded within the training process (Karniadakis et al., 2021; Meng et al., 2025). It has been applied across a wide range of domains, including weather and climate modelling (Kashinath et al., 2021), daily snow and ice albedo reconstruction (Ye et al., 2023), snowpack modelling (Maharjan et al., 2025; Zhao et al., 2026), and the simulation of climate-driven runoff shifts in alpine catchments (Zhong et al., 2023). PIML offers a promising framework for reconstructing snow cover time series, as spatiotemporal variability in snow cover reflects underlying physical processes such as accumulation and ablation. Incorporating these processes as constraints can improve model realism and predictive skill (Meng et al., 2025). Achieving this requires a reconstruction workflow that mimics the iterative solution strategies of physically-based numerical models. In this framework, the evolving state of the system provides context for estimating the probability of snow presence or absence at subsequent timesteps.

In this study, we present snowMapper v1.0, a modular, PIML-driven model for reconstructing daily snow cover at 100 m spatial resolution. Using this framework, we generate a comprehensive 41-year reconstruction of snow cover across key mountain massifs in Greece, drawing on four decades of satellite observations. We then evaluate the reconstructed datasets to identify climatologically significant trends and interpret these changes in relation to both local atmospheric conditions and large-scale modes of climate variability. In this way, we contribute new insights into the largely unexplored dynamics of snow cover in the Greek mountains.

2. Methods

2.1 Study area

In Greece, winter precipitation exhibits pronounced temporal and spatial variability due to the interaction between synoptic circulation patterns and complex topography. The Pindus Mountains form a major climatic divide, separating the wetter western mainland from the drier eastern regions. During meridional circulation, cold northeasterly flows - often triggered by Siberian or central European blocking anticyclones - bring precipitation to eastern Greece, particularly in mid to late winter (Bartzokas et al., 2003). Conversely, zonal circulation dominates in the west, producing longer and more frequent precipitation events, with limited spillover to the eastern Pindus (Bartzokas et al., 2003). Analysis of surface station data from 2010-2023, indicates that heavy winter precipitation events (R20 > 20 mm day^{-1}) occur most frequently over western Greece (Kotroni et al., 2025). Snow cover typically persists from November to May, with isolated patches lasting into mid-summer (Masloumidis et al., 2025).

The study area was delineated using the hierarchical inventory of the world's mountains, Global Mountain Biodiversity Assessment (GMBA) v2 product (Snethlage et al., 2022a, b). The dataset was clipped to the Greek national borders, and ten mountain massifs across the mainland with maximum elevations > 2,000 m a.s.l. were selected for snow-cover reconstruction and climatological analysis (Fig. 1).

Water was masked using the Joint Research Centre's Global Surface Water dataset v1.4 (Pekel et al., 2016), based on the maximum extent observed over the dataset period, 1984-2022. Snow cover detection over forested areas presents a known challenge for optical remote sensing (Gascoin et al., 2024; Muhuri et al., 2021), and therefore a forest mask was applied using the 2015 Tree Cover Density 100 m dataset (European Environment Agency, 2018). Grid cells were masked when tree cover density was ≥ 50% (Barrou Dumont et al., 2025). Lastly, an elevation mask was applied, discarding areas lower than 700 m a.s.l., based on the Shuttle Radar Topography Mission (SRTM) digital elevation dataset (DEM) v3 (Farr et al., 2007).

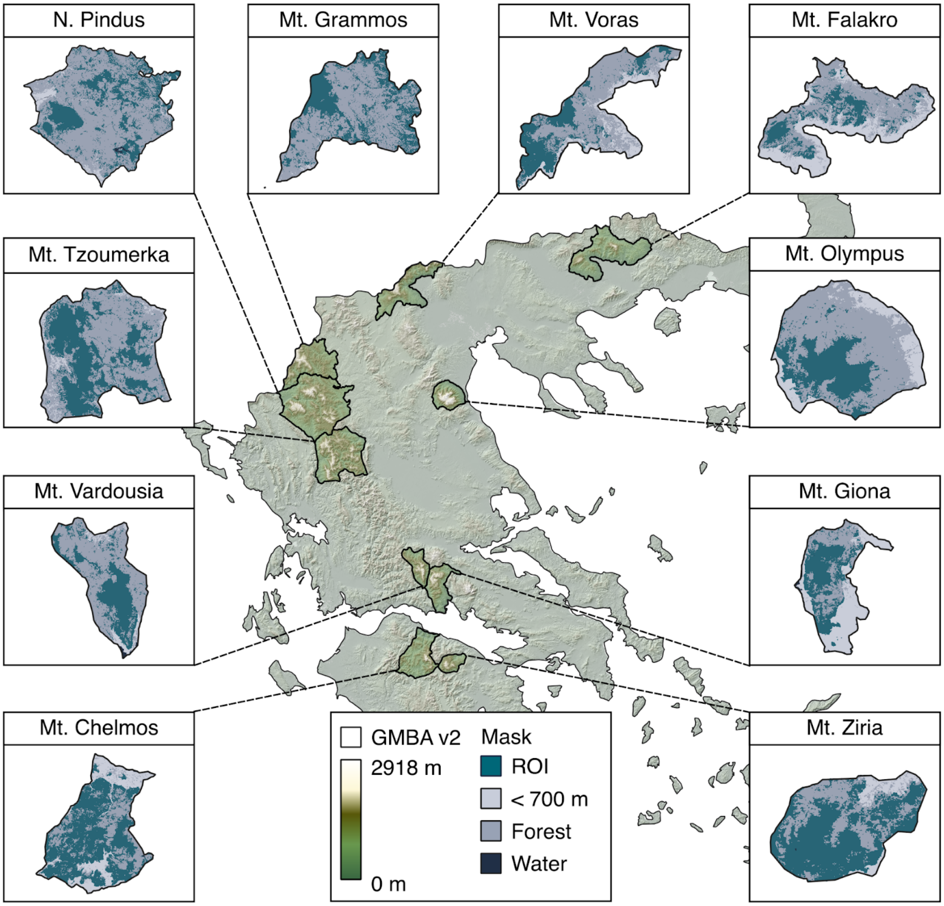

Figure 1: Locations of the ten Greek mountain massifs analysed in this study, together with their regions of interest (ROIs) for snow-cover reconstruction, delineated following the application of elevation, forest, and water masks.

2.2 snowMapper model overview

snowMapper is an iteratively-solved, PIML-driven model developed in this study for reconstructing daily snow cover (Fig. 2). The model is trained on in situ data, forced by reanalysis-derived meteorological conditions, and updated through direct insertion of binary snow cover from available high-resolution satellite imagery. Its modular structure comprises of three main steps (Fig. 2):

- Step 1: Preprocessing This includes the preparation of (a) satellite imagery (Section 2.3.1), (b) meteorological forcing data (Section 2.3.2), (c) terrain data (Section 2.3.3), and (d) in situ training data (Section 2.3.4), followed by (e) training of the machine learning classifier (Section 2.3.5).
- Step 2: Snow cover reconstruction. This step consists of (a) model initialisation (Section 2.4.1) and (b) model execution (Section 2.4.2).
- Step 3: Validation and correction. This involves (a) the extraction of evaluation metrics and a post-processing validation routine (Section 2.5), and (b) the insertion of observed snow cover values (Section 2.4.3).

The entire process is performed using the cloud-based resources of Google Earth Engine through the Python API (Gorelick et al., 2017). The model input data and preprocessing, model development and snow reconstruction, and model validation and direct insertion of observations are detailed in the following subsections.

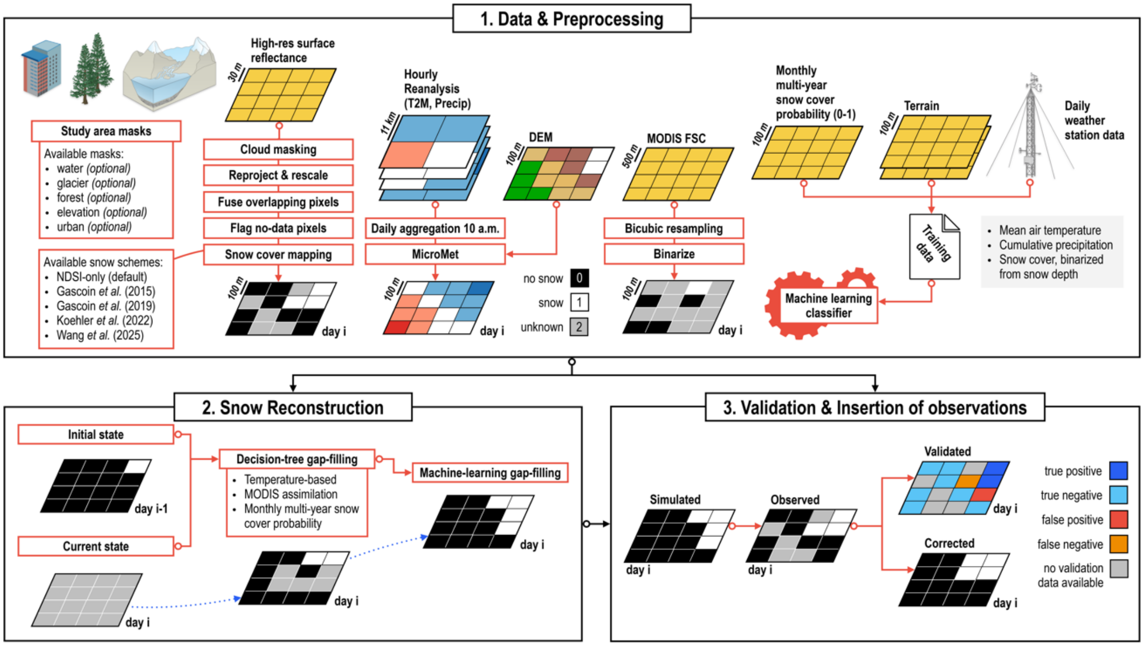

Figure 2: Schematic of the snowMapper v1.0 model.

2.3 Data & pre-processing

2.3.1 Satellite imagery

We imported atmospherically corrected surface-reflectance imagery from the following high-resolution satellite sensors available in the Google Earth Engine Data Catalogue: Landsat 4/5 TM, Landsat 7 ETM+, Landsat 8 OLI, Landsat 9 OLI-2, and Sentinel-2A/B/C MSI. First, pre-processing was performed separately on each image to apply sensor-specific scaling factors and to mask cloud-covered pixels. Clouds masking used CFMask (Foga et al., 2017) for the Landsat sensors and Cloud Score+ (Pasquarella et al., 2023) for Sentinel-2, with a probability threshold of 60% (default) for the latter. All imagery was then resampled to 100 m resolution and aligned to the Greek Grid (EPSG:2100). Daily overlapping scenes were fused using the median reflectance of coincident pixels.

Various methods have been developed to derive binary snow cover from surface reflectance (Barella et al., 2022; Bousbaa et al., 2022; Gascoin et al., 2015, 2019; Koehler et al., 2022; Poussin et al., 2024; Wang et al., 2025), most of which employ the Normalised Difference Snow Index (NDSI), computed from the green and shortwave infrared (SWIR) bands (Eq. 5) and a decision tree of thresholds.

$$NDSI = \frac{Green - SWIR}{Green + SWIR} \tag{5}$$

While spatiotemporally optimized NDSI thresholds can improve classification performance (Härer et al., 2018; Poussin et al., 2023), their calibration typically relies on in situ observations, which are unavailable in our study area. We therefore adopt a fixed NDSI threshold, which has been shown to provide high accuracy in binary snow cover classification while maintaining consistent performance across time and space (Gascoin et al., 2015; Koehler et al., 2022; Moazzam et al., 2022). We empirically modified the approach used by Gascoin et al. (2015), classifying a pixel as snow-covered when NDSI > 0.4 and red-band reflectance < 0.1. This produced binary snow cover maps of snow presence (1) and snow absence (0). Pixels lacking reflectance data due to cloud masking, Landsat 7 SLC-off gaps, or missing imagery were flagged (2) for reconstruction.

Reflectance differences between sensors were assumed to be negligible, and therefore, no inter-sensor reflectance calibration was applied. Several previous studies have created multi-sensor snow cover products without such calibration (Barrou Dumont et al., 2025; Bousbaa et al., 2022; Gascoin et al., 2019; Koehler et al., 2022; Moazzam et al., 2022; Poussin et al., 2024; Wayand et al., 2018), while Rumpf et al. (2022) reported that applying sensor calibrations did not affect their results.

We then used all binary snow-cover maps to compute monthly multi-year snow-cover probabilities ($\overline{SC_m}$) (Poussin et al., 2024; Wayand et al., 2018), representing the likelihood, from 0 (snow-free) to 1 (snow-covered), that a grid cell contains snow in a given month (Fig. A2) (Eq. 6).

$$\overline{SC}_m = \frac{\sum SC_{d\in m}}{N_m} \tag{6}$$

Lastly, we incorporated MODIS Terra imagery. Fractional snow cover (FSC) from the MOD10A1 V6.1 Snow Cover Daily Global product (Hall and Riggs, 2015) was filtered to retain only pixels with the highest quality score (bit 0 under Basic Quality Assessment). These data were bicubically resampled from 500 m to 100 m, and then binarized using an empirically based 50% FSC threshold (Notarnicola, 2020; Shen et al., 2025). Although several methods exist for downscaling MODIS to higher resolutions (Bousbaa et al., 2024; Kollert et al., 2024; Mahanthege et al., 2024; Revuelto et al., 2021), bilinear – and, by extension, bicubic – resampling has been shown to provide a robust and computationally efficient method for this purpose (Kollert et al., 2024). MODIS Aqua-derived snow cover was not used due to its lower snow detection accuracy relative to MODIS Terra (Gascoin et al., 2015), as well as its later overpass time (~13:30 compared to ~10:00 for MODIS Terra, Sentinel-2, and Landsat). This temporal offset causes inconsistencies in the calibration of the meteorological forcing data described in the following subsection.

Given its coarser native spatial resolution, MODIS was used in an auxiliary role for gap-filling, rather than to supplement the primary observational dataset, from the Landsat and Sentinel-2 satellites. Although it extends back only to February 2000, we anticipated that integrating MODIS Terra data would significantly enhance reconstruction accuracy during snowMapper's decision-tree gap-filling stage.

2.3.2 Reanalysis

The land component of the fifth generation of European ReAnalysis, ERA5-Land, produced by the European Centre for Medium-Range Weather Forecasts (ECMWF), provides gridded global hourly meteorological data at 0.1° spatial resolution (Muñoz-Sabater et al., 2021). We aggregated the hourly fields into daily values running from 11:00 on day i to 10:00 on day i+1. This window was chosen over the standard midnight to midnight period because 10:00 corresponds closely to the typical satellite overpass time in the region, ensuring that each daily composite reflects the most relevant and recent meteorological conditions for the associated satellite image.

We used daily aggregates of mean near-surface air temperature and total precipitation to drive the quasi-physically based meteorological downscaling model MicroMet (Liston and Elder, 2006b). MicroMet applies monthly air temperature lapse rates and precipitation adjustment factors, calculated for the Northern Hemisphere by Kunkel (1989) and Thornton et al. (1997), respectively, together with a DEM at the target resolution. We first resampled ERA5-Land data to the target resolution using the nearest-neighbour interpolation. Downscaling was then performed using the 30 m SRTM DEM v3 (Farr et al., 2007) resampled bicubically to 100 m, together with the respective MicroMet temperature and precipitation functions. While other downscaling approaches may provide higher accuracy (Fiddes and Gruber, 2014; Sebbar et al., 2023), MicroMet strikes a good balance between realism and computational efficiency (Fig. A1), and has been successfully used in similar applications (Choler et al., 2024; Liston and Elder, 2006a).

In addition to air temperature (T) and precipitation (P), we derived four additional daily variables at 100 m resolution: heating degrees (HD; Eq. 1), cooling degrees (CD; Eq. 2), precipitation occurring under heating conditions (P^{HD}; Eq. 3), and precipitation occurring under cooling conditions (P^{CD}; Eq. 4):

$$HD = max(0, T - T_{base}) \tag{1}$$

$$CD = max(0, T_{base} - T) \tag{2}$$

$$P^{HD} = \begin{cases} P, if\ T > T_{base} \\ 0, if\ T < T_{base} \end{cases} \tag{3}$$

$$P^{CD} = \begin{cases} P, if\ T < T_{base} \\ 0, if\ T > T_{base} \end{cases} \tag{4}$$

where $T_{base} = 0$ ºC.

2.3.3 Terrain

Elevation was sourced from the 100 m bicubically resampled SRTM DEM. We also incorporated two SRTM-derived terrain variables from Theobald et al. (2015): the multi-scale topographic positioning index (mTPI; 270 m resolution) and the Continuous Heat-Insolation Load Index (CHILI; 90 m resolution), both of which were bicubically resampled to 100 m. mTPI distinguishes ridge from valley forms, while CHILI characterises the effect of insolation and topographic shading on surface energy balance and evapotranspiration, both contributing valuable ancillary information relevant for modelling snow-cover dynamics.

2.3.4 In situ data

The snowMapper classifier requires in situ data for training. For this purpose, we used in situ observations of snow-depth, air temperature, and precipitation from the European Climate Assessment & Dataset (ECA&D) project (Klein Tank et al., 2002). We selected all 49 stations located within the Mediterranean region, primarily in the Pyrenees and European Alps (Fig. A3a), since no data were available for Greece. Daily in situ observations were preferred over daily ERA5-Land reanalysis data because they provide higher accuracy and greater sensitivity to local scale variability at the 100 m resolution of the model (Monteiro and Morin, 2023), which is crucial for training a PIML classifier (Meng et al., 2025).

First, we binarized snow depth measurements at the 1 cm threshold (Barrou Dumont et al., 2025; Pan et al., 2024; Sadeghi et al., 2025). To ensure accurate determination of snow cover onset, melt-out, and duration—and the associated meteorological conditions relevant to accumulation and ablation—the dataset was filtered to retain only continuous records. A restrictive sequential filtering routine excluded sections of daily data when:

i. a snow-cover period lacked a traceable first day (i.e., no snow-absence observation immediately preceding the first snow-presence day); or

ii. there was a gap in the record ≥ 1 day during a snow-cover period.

For the remaining continuous snow-cover periods, additional daily metadata variables were computed, including the cumulative snow cover on day d_i (ΣSC), heating degrees (ΣHD), cooling degrees (ΣCD), precipitation under warming conditions (ΣP^{HD}), and precipitation under cooling conditions (ΣP^{CD}), following Eq. (7),

$$\Sigma X_{d_i} = \left(\Sigma X_{d_{i-1}} + X_{d_i}\right) \times SC_{d_i} \tag{7}$$

for X in $[SC,\ HD,\ CD,\ P^{HD},\ P^{CD}]$. By multiplying the sum of X with the current binary snow cover condition (SC), we ensure that cumulation occurs only on days when snow is present, while in the absence of snow, each cumulative variable is reset to zero. This approach ensures that the five cumulative variables influence snow cover processes, but not snow-free conditions.

Each station's dataset was further augmented with the SRTM-derived terrain indices, mTPI and CHILI, with elevation taken directly from each station's metadata, as well as the monthly multi-year snow cover probability corresponding to the station's grid cell. To maintain a purely physics-informed classifier, the training dataset excluded both the geographic coordinates of the stations and the dates of measurement.

We categorised data points into one of the following four snow cover phases (Eq. 8):

$$SC_{d_i}^{phase} = \begin{cases} no\ snow, if\ SC_{d_i} = 0\ and\ \Sigma SC_{d_{i-1}} = 0 \\ new\ snow, if\ SC_{d_i} = 1\ and\ \Sigma SC_{d_{i-1}} = 0 \\ snow, if\ SC_{d_i} = 1\ and\ \Sigma SC_{d_{i-1}} \geq 1 \\ melted\ snow, if\ SC_{d_i} = 0\ and\ \Sigma SC_{d_{i-1}} \geq 1 \end{cases} \tag{8}$$

We then sampled approximately 10,000 daily data points from all available stations, using stratified sampling to ensure an approximately even representation across different elevation bands, mTPI and CHILI values, monthly multi-year snow cover probabilities, and snow cover phases (Fig. A3b).

2.3.5 Machine learning classifier

Random forests (Breiman, 2001) are one of the most widely used machine learning models in land-surface and atmospheric research, often chosen for their robustness, high accuracy and relatively low computational cost compared to other statistical methods (Belcore et al., 2020; Hu and Shean, 2022; Mahanthege et al., 2024; Sheykhmousa et al., 2020). In our case, the classifier was configured with 30 trees following an error matrix sensitivity analysis during trial runs. The minimum leaf population and a bag fraction were set to their default values of 1 and 0.5, respectively. This configuration ensures that each tree is trained on a random 50% bootstrap sample of the available data, while terminal nodes can contain a single observation, thereby maximizing the model’s ability to capture local variability in snow–land-surface relationships. Figure 3 shows the relative importance assigned by the classifier to each variable in the training dataset.

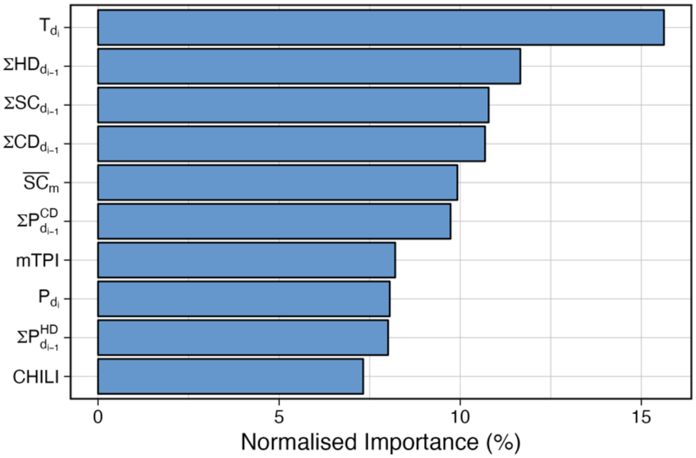

Figure 3: Normalised importance of each predictor variable in the snowMapper random forest classifier.

2.4 Snow cover reconstruction

2.4.1 Model initialisation

We selected October as the initialisation month for each annual snowMapper run. Within snowMapper, cloud-masked surface reflectance satellite images from October of a given year were combined into a single mean-reflectance composite. This composite was then converted to a binary snow cover map using the NDSI approach described in Section 2.3.1, with any remaining gaps assigned a snow-free value (0). The last day of October was set as the date of this initial-state image, and meteorological conditions of that day, along with terrain variables and the monthly multi-year snow cover probability, were added as metadata. Initial states of cumulative variables were calculated based on these initial snow cover conditions using Eq. (7).

2.4.2 Model run

snowMapper reconstructs daily snow cover conditions on a cell-by-cell basis across the grid through sequential daily iterations, using the previous day's (d_{i-1}) cumulative variables, the current day's (d_i) meteorological variables, the current month's (m) multi-year snow cover probability, and the terrain variables. In the first step of reconstruction, a three-stage sequential decision-tree gap-filling algorithm is applied.

For a given day (d_i) and grid cell, snow cover is first inferred from the previous day's state (d_{i-1}), combined with meteorological conditions: if snow was present on (d_{i-1}) and the current-day air temperature is ≤ 0 ºC, snow cover is maintained; conversely, if snow was absent on (d_{i-1}), current-day precipitation is zero and air temperature is > 0 ºC, snow-free conditions are maintained. In the second stage, any remaining no-data grid cells are filled using the down-sampled clear-sky MODIS snow cover data. In the third stage, remaining empty grid cells are classified based on multi-year snow cover probabilities following Poussin et al. (2024): cells with a monthly snow cover probability of 1 are classified as snow-covered, while those with a probability of 0 are classified as snow-free. The full decision tree is described in Eq. (9):

$$SC_{d_i} = \begin{cases} 1, if\ SC_{d_{i-1}} = 1\ and\ T_{d_i} \leq T_{base} \\ 1, if\ SC_{d_i}^{MODIS} = 1 \\ 1, if\ \overline{SC}_m = 1 \\ 0, if\ SC_{d_{i-1}} = 0\ and\ T_{d_i} > T_{base}\ and\ P_{d_i} = 0\ mm \\ 0, if\ SC_{d_i}^{MODIS} = 0 \\ 0, if\ \overline{SC}_m = 0 \end{cases} \tag{9}$$

In the second step of reconstruction, all remaining no-data grid cells are assigned snow or no-snow values using the random forest classifier.

2.4.3 Direct insertion of observations

Once the classifier has filled all remaining gaps, available clear-sky Landsat- or Sentinel-derived snow cover observations are used to replace the corresponding predicted values. The cumulative variables for the current day are then updated based on the latest snow cover conditions using Eq. (7). snowMapper then progresses sequentially to the next day, iterating daily until the end of the simulation period.

2.4.4 Final output

Once snowMapper has fully reconstructed daily snow cover across the domain and simulation period, we aggregated binary snow cover values to monthly means for each massif. The resulting variable represents monthly spatiotemporal fractional snow cover (FSC) at the massif scale. Although this aggregation reduces the dimensionality of the dataset, such that different combinations of daily snow cover extent and duration within a month may produce identical monthly FSC values, the metric implicitly captures both spatial extent and temporal persistence of snow cover. This is consistent with hydrological perspectives, in which the value of the snowpack depends on both the volume of water stored as snow and the duration of its storage in that frozen form (Aragon and Hill, 2024). Accordingly, spatiotemporal FSC provides an integrated measure of snow cover extent and duration, offering a versatile metric for dataset evaluation and analysis.

2.5 Model evaluation & bias correction

After reconstructing each day's snow cover, but prior to the direct insertion of available Landsat- or Sentinel-derived observations, model performance was evaluated at the grid-cell-level against these clear-sky satellite observations on a day-to-day basis (Fig. 2). All available observations were used for validation, as they remained independent at this step and were only replaced after evaluation, following the process described in Section 2.4.3. Cells were classified as 'true positive' (tp), 'true negative' (tn), 'false positive' (fp), or 'false negative' (fn), based on the conditions outlined in Eq. 10:

$$Evaluation_{d_i} = \begin{cases} tp, if\ SC_{d_i}^{observed} = 1\ and\ SC_{d_i}^{simulated} = 1 \\ tn, if\ SC_{d_i}^{observed} = 0\ and\ SC_{d_i}^{simulated} = 0 \\ fp, if\ SC_{d_i}^{observed} = 0\ and\ SC_{d_i}^{simulated} = 1 \\ fn, if\ SC_{d_i}^{observed} = 1\ and\ SC_{d_i}^{simulated} = 0 \end{cases} \tag{10}$$

At the end of the model run, we cumulate these daily grid cell-level evaluations across each month and massif, and calculate monthly performance metrics: accuracy (Eq. 11), snow overestimation (Eq. 12), and snow underestimation (Eq. 13) (Parajka and Blöschl, 2008):

$$Accuracy_{(m,y)} = \frac{\sum_{i=1}^{N(m,y)}(tp_{(i,m,y)}+tn_{(i,m,y)})}{\sum_{i=1}^{N(m,y)}(tp_{(i,m,y)}+tn_{(i,m,y)}+fp_{(i,m,y)}+fn_{(i,m,y)})} \tag{11}$$

$$Overestimation_{(m,y)} = \frac{\sum_{i=1}^{N(m,y)}(fp_{(i,m,y)})}{\sum_{i=1}^{N(m,y)}(tp_{(i,m,y)}+tn_{(i,m,y)}+fp_{(i,m,y)}+fn_{(i,m,y)})} \tag{12}$$

$$Underestimation_{(m,y)} = \frac{\sum_{i=1}^{N(m,y)}(fn_{(i,m,y)})}{\sum_{i=1}^{N(m,y)}(tp_{(i,m,y)}+tn_{(i,m,y)}+fp_{(i,m,y)}+fn_{(i,m,y)})} \tag{13}$$

We bias-corrected the reconstructed monthly FSC values using an approach inspired by the trend-preserving delta-change method (Matiu and Hanzer, 2022). First, we calculated the representativeness index (RI) (Koehler et al., 2022), which quantifies the percentage of available observations in a given month for a given GMBA mountain area relative to the total number of grid cells in that month and area (Eq. 14):

$$RI_{(m,y)} = \frac{N^{obs}_{(m,y)}}{N^{all}_{(m,y)}} \tag{14}$$

Second, we removed all instances where the RI < 0.015, as such a low proportion of observations was considered insufficient for reliable validation and subsequent bias correction. This threshold corresponds roughly to having a clear-sky view of half the area's grid cells on a single day within a month. Third, for each massif over the study period, we calculated the monthly mean underestimation ($\bar{U}_m$) and overestimation ($\bar{O}_m$) metrics. Fourth, these values were then used to correct the reconstructed FSC according to Eq. (15):

$$FSC_{corrected_{(m,y)}} = FSC_{m,y} + \min\left(U_{(m,y)}, \bar{U}_m\right) - \min\,(O_{(m,y)}, \bar{O}_m) \tag{15}$$

Finally, we converted the corrected monthly FSC values to monthly snow-covered area (SCA) by multiplying each value by the masked area (km^2) of the respective massif (Section 2.1).

2.6 Climatological analysis

We performed climatological analyses both across the entire study area and at the massif scale.

Ten-year moving averages of the bias-corrected SCA time-series were calculated for each calendar month of the snow season (November - May) to smooth interannual variability. For each month, we applied the Mann-Kendall test to identify trends and we estimated their slope using the Theil-Sen method, both for individual massifs and for all 10 massifs collectively. To facilitate inter-month comparison Sen's slopes were normalised by dividing by the mean SCA for that month, yielding the fractional annual change in SCA relative to the mean snow-covered area rather than to the total reconstructed area of each massif.

We calculated SCA anomalies relative to the 1984-2025 monthly means and identified extreme high and low snow-cover events based on the monthly 80th and 20th percentile thresholds. Extremes were grouped by snow season, and aggregated as means for magnitude and as counts for frequency. The autocorrelation-sensitive modified Mann-Kendall test was then applied (Hamed and Ramachandra Rao, 1998) to identify trends in both (Li et al., 2025).

Using the unsmoothed SCA time-series for each month, we examined correlations with climate and climate variability by performing Pearson's tests against: (a) mean air temperature, (b) cumulative precipitation, (c) North Atlantic Oscillation (NAO) index, (d) Atlantic Multidecadal Oscillation (AMO) index, and (e) Arctic Oscillation (AO) index.

Finally, each month's unsmoothed SCA time-series was split into two partially overlapping 21-year subperiods: 1984/1985-2004/2005 and 2004/2005-2024/2025. For each subperiod, we calculated the mean and standard deviation and applied Levene's test to assess differences in SCA variability.

For all statistical tests, we report statistical significance at the 95% confidence level ($p < 0.05$).

3. Results

3.1 snowMapper evaluation

The 41-year daily snow cover reconstruction produced by snowMapper was based on 1.1 billion clear sky observations (image pixels) from Landsat and Sentinel-2 (Fig. 4), representing just 7.6 % of the final dataset. The remaining 92.9 % of snow cover values were reconstructed through the model's two-step gap-filling approach: the decision-tree algorithm (44.9 %) and the machine learning classifier (47.5 %).

A clear annual cycle is evident in the proportion of grid cells reconstructed by the decision-tree algorithm, which is higher during winter months, compared to the machine learning classifier. This pattern reflects seasonal variation in the reliability of the air temperature - snow cover relationship. In winter, high altitudes temperatures are often ≤ 0 °C, enabling the decision-tree to confidently classify snow presence based on the previous day's conditions. However, during snow transition periods - late autumn/early winter and late spring - snow presence may not coincide with freezing temperatures preventing the first decision-tree criterion (Eq. 9) from being satisfied.

The fraction of values gap-filled by the decision-tree algorithm increased after 2000 due to the launch of MODIS Terra, while the availability of clear-sky observations has risen more than fivefold since the launch of Sentinel-2 during the last decade of the study period.

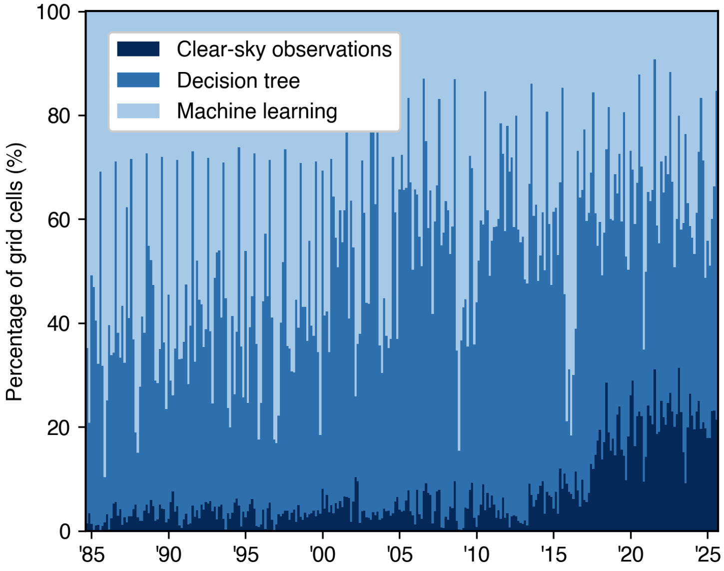

Figure 4: Monthly proportions of original clear-sky grid cells and gap-filled grid cells reconstructed by the decision-tree and machine-learning algorithms. For each month-year, 100% represents the sum of all grid cells of the study area across all days of that given month.

Overall, across the ten massifs, the daily snow cover reconstruction achieved an average accuracy of 93 % (Fig. 5). Of the remaining 7 % of misclassified cases, snow presence was underestimated in 4.7 % (snow present but classified as absent) and overestimated in 2.3 % (snow absent but classified as present). Model performance declines slightly during the transitional months of the snow season compared to mid-winter, primarily due to a systematic underestimation of snow cover.

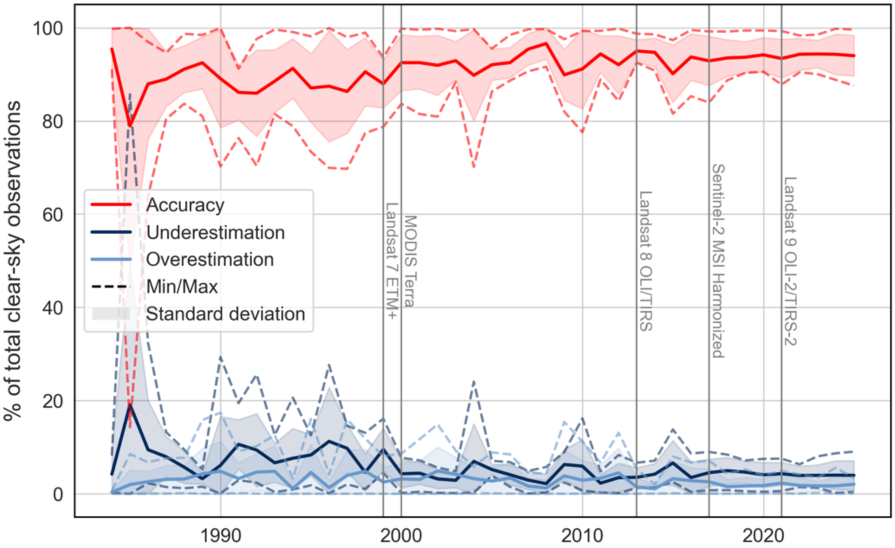

Figure 5: Skill of snowMapper across the entire study area, calculated monthly through Eq. (11)-(13), and presented as yearly means (solid lines), minimums/maximums (dashed lines), and standard deviations (shading). Vertical lines mark the beginning of a new satellite dataset, from the ones included in the reconstruction configuration. Also included in the reconstruction but not displayed in the above graph is Landsat 4-5 TM launched at the start of the time-series. Massif-level evaluation is provided in Fig. A4.

3.2 Mountain snow cover trends & anomalies

Across the Greek mountains, SCA has exhibited a steep declining trend over the past four decades, both for the overall snow season (-8.64 km^2 yr^{-1}) and for each month from November through to May (Fig. 6). Trends are statistically significant for all months except February (p=0.1). The steepest absolute declines occur in December (-18.9 km^2 yr^{-1}), followed by March (-13.7 km^2 yr^{-1}), January and April (both -7.9 km^2 yr^{-1}), February (-7.3 km^2 yr^{-1}), November (-5.9 km^2 yr^{-1}), and May (-0.6 km^2 yr^{-1}). When these rates are normalised by each month's mean SCA (1984-2025), the greatest proportional losses emerge at the beginning and end of the snow season: November (-3.0 % yr^{-1}), December (-1.9 % yr^{-1}), April (-1.6 % yr^{-1}), May (-1.3 % yr^{-1}), and March (-1.1 % yr^{-1}). In contrast, the mid-winter months show markedly smaller fractional declines, with January at -0.5 % yr^{-1} and February at -0.4 % yr^{-1}.

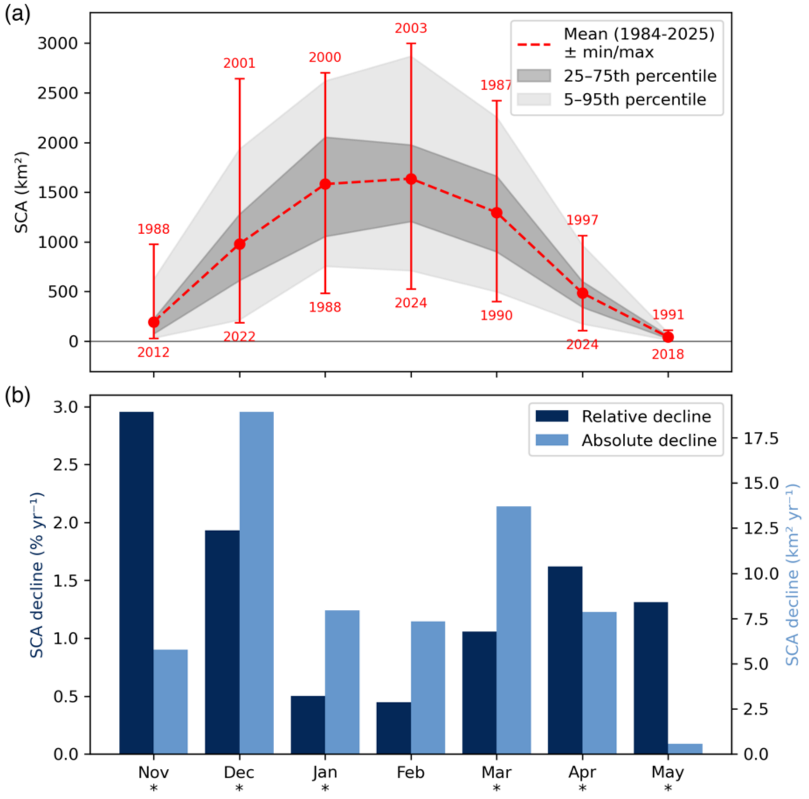

Figure 6: (a) Monthly mean, minimum, maximum, and 25-75th and 5-95th percentiles of snow cover area (SCA) across the snow season. (b) Decline in SCA, shown in absolute and relative terms, calculated based on the mean SCA for the period 1984-2025. Asterisks (*) denote statistically significant trends. All metrics are calculated for the entire study area.

Beyond the overall downward trends, the monthly evolution of SCA exhibits three distinct temporal patterns (Fig. 7):

- **Steady decline:** November shows a consistent, approximately linear decrease in SCA throughout the past four decades.
- **Mid-period peak followed by sustained decline:** December and March show an initial rise in SCA, reaching peaks in the early 2000s and late 1990s, respectively, followed by a steady decline over the past two decades.
- **Rise to a peak followed by a rapid, decade-long drop:** January, February, April and May display an early period increase culminating in a peak, after which SCA declines sharply over an interval of approximately ten years. These periods of decline occur between 2005-2013 for January, 2008-2021 for February, 2000-2010 for April, and 1991-2001 for May. For April and May, SCA subsequently stabilises – though with some variability, particularly notable for January - at a substantially lower level.

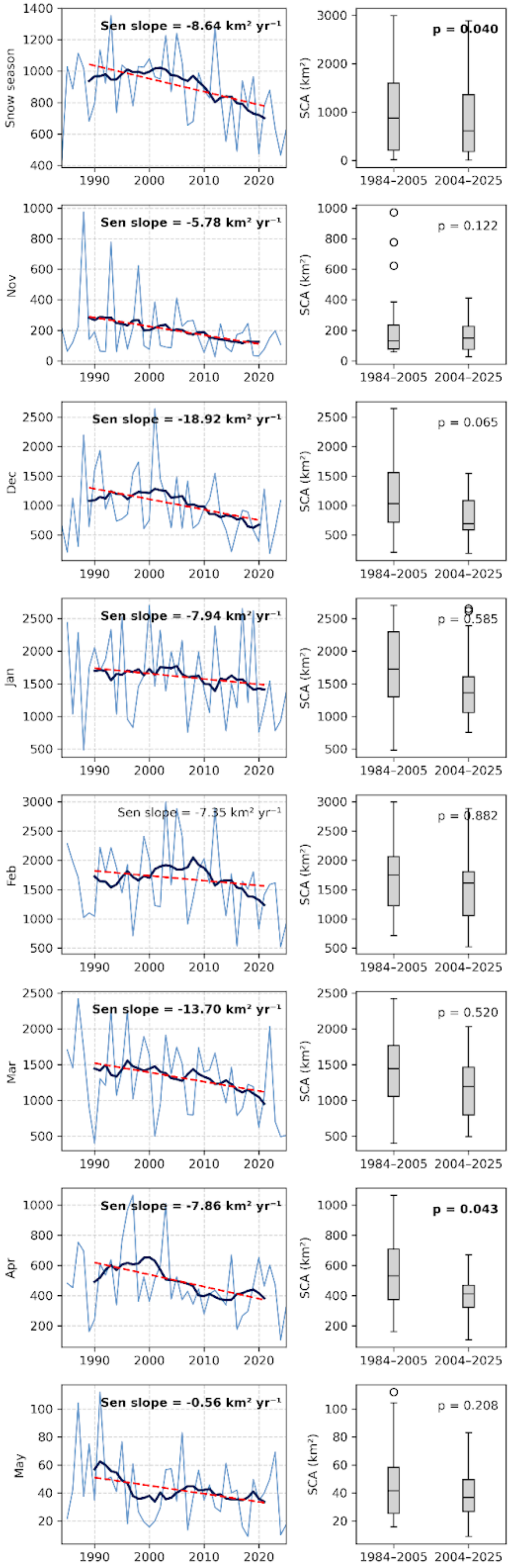

Snow season
Sen slope = -8.64 km² yr⁻¹
p = 0.040
Nov
Sen slope = -5.78 km² yr⁻¹
p = 0.122
Dec
Sen slope = -18.92 km² yr⁻¹
p = 0.065
Jan
Sen slope = -7.94 km² yr⁻¹
p = 0.585
Feb
Sen slope = -7.35 km² yr⁻¹
p = 0.882
Mar
Sen slope = -13.70 km² yr⁻¹
p = 0.520
Apr
Sen slope = -7.86 km² yr⁻¹
p = 0.043
May
Sen slope = -0.56 km² yr⁻¹
p = 0.208
SCA (km²)
1990
2000
2010
2020
1984–2005
2004–2025

Figure 7: Yearly SCA time-series (light blue lines), 10-year-smoothed SCA (dark blue lines), and overall trends (dashed red lines), along with differences in variability between two 21-year sub-periods across the entire study area. Bold text indicates statistically significant trends (line chart: Mann-Kendall/Sen's slope) and significant differences in variability (boxplot: Levene's test). Massif-level trends and variability differences are shown in Figs. A5 and A6.

Trend analysis of the monthly SCA anomalies across the study area and time period reveals a significant decline in both the magnitude and frequency of extremely high snow-cover instances, while no significant trend is observed for extremely low snow cover instances (Fig. 8).

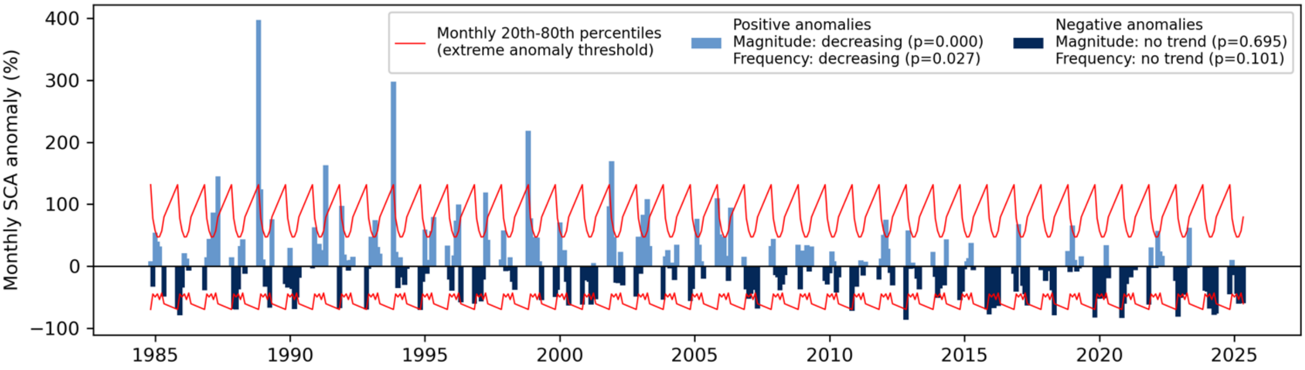

Figure 8: Monthly SCA anomalies (%) relative to the 1984-2025 period, and Mann-Kendall trends the magnitude and frequency of extremely high and low snow cover, based on the monthly 80th and 20th percentiles, respectively.

3.3 Correlations

Pearson's correlation analyses show that, across the entire study area, SCA is more strongly associated with temperature and precipitation than with regional climate indices (Fig. 9). Air temperature displays strong and statistically significant anticorrelations with SCA in all months, whereas precipitation shows moderate to strong positive correlations during November-December and February-March. Among the climate indices, a significant anticorrelation with NAO is found only in February, while both the AO and AMO show significant anticorrelations in February and March. These patterns are broadly consistent at the individual massif scale, with only minor shifts (±1 month) in the timing of significant correlations with precipitation and the climate indices (Fig. A7). At the massif scale, February is the only month in which all ten massifs display a significant positive correlation between SCA and precipitation, while March is the only month in which all ten massifs display a significant negative correlation between SCA and AMO. Among the three climate indices, the AO exhibits the clearest and most coherent behaviour, with positive correlations across all ten massifs in early winter (Dec-Jan) and negative correlations in the later months (Feb-Apr), significant only for the massifs located in the northern parts of mainland Greece (Fig. A7).

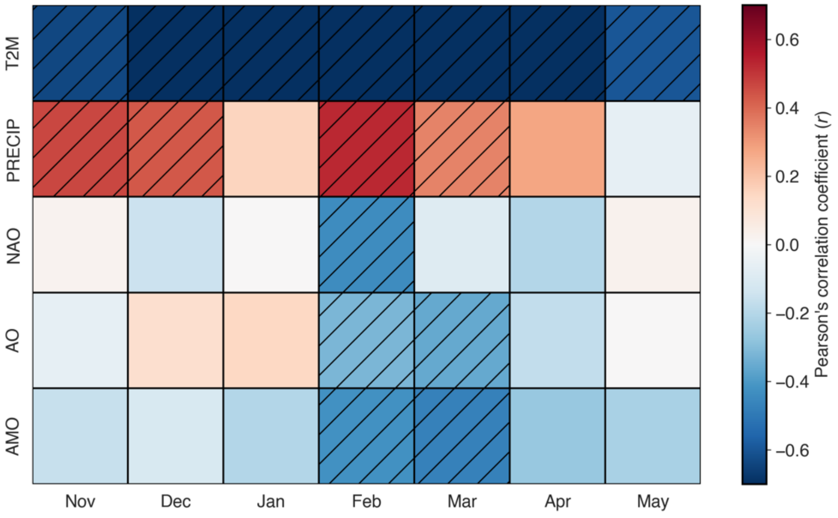

Figure 9: Pearson correlation coefficients between SCA and monthly mean 2 m air temperature (T2M), monthly cumulative precipitation (PRECIP), and major regional climate indices (NAO, AO, AMO) across all massifs in the study area. Red and blue indicate positive and negative correlations, respectively, and hatching denotes statistically significant values.

3.4 Variability

Levene's test, applied to the two 21-year sub-periods (1984/1985-2004/2005 and 2004/2005-2024/2025) for each month, revealed no significant difference in the variability of total SCA between the two sub-periods. This result is consistent both across the entire study area and at the scale of the individual massifs (Fig. A6).

4 Discussion

4.1 Trends, drivers & implications of snow cover reduction

Over the past four decades, ten of the highest massifs in Greece have undergone a rapid decline in SCA throughout the snow season, amounting to an average reduction of 57.5 % (± 1.4 %) at the end of the study period relative to the 1984-2025 mean. Rates of decline are greatest at both the beginning and end of the season, consistent with global evidence for a shortening of snow-cover duration driven by later onset and earlier melt-out dates (Notarnicola, 2020). Snow cover declined steadily in November, December and March across most of the record, whereas January, April and May show a pronounced drop around the turn of the century (±10 years). In contrast, the decline in February becomes apparent only within the past decade. Corresponding patterns are observed in the extremely positive SCA anomalies, which display a marked shift - both in frequency and magnitude - toward milder conditions, consistent with the reported decline in winter cold spell frequency (Tringa et al., 2022) and the overall warming trends (Fig. A8).

Although our analysis incorporates satellite-derived snow cover data, these observations are used within snowMapper primarily to constrain the simulated snow cover and limit the temporal propagation of gap-filling errors. Therefore, the reported trends are unlikely to be biased by the increasing availability of satellite observations in recent decades (Bayle et al., 2024). This is because the analysis is based not on irregularly captured satellite imagery, but on monthly aggregates derived from reconstructed daily snow cover maps.

To compare our results with existing literature on Greece and with other, better-studied mountain ranges, we repeated the trend analysis workflow described in Section 2.6 using the snow-cover phenology dataset of Notarnicola (2024a, b). Because that dataset is based on MODIS and begins only in 2000, we filtered our own dataset to the same time period, and re-ran the trend analysis. This revealed, once again, a significant decline in SCA, with a Sen's slope, normalised to the mean snow cover area, of -2.3 % yr^{-1}. The snow loss estimated from the Notarnicola (2024a) dataset was of comparable magnitude (-1.8 % yr^{-1}), with a slight underestimation likely due to methodological differences: our analysis is restricted to the snow season (Nov-May), whereas Notarnicola (2024b) considers the full hydrological year.

Using the same dataset, comparable rates of snow loss over 2000-2023 are evident for other mountains with Mediterranean or Mediterranean-like climates and marginal snowpacks (Table 1). In contrast, major mountain ranges with more persistent snowpacks exhibit far slower declines (e.g., Rockies: -0.02% yr^{-1}; Hindu Kush Himalaya: -0.04% yr^{-1}; Cordillera Central: -0.9% yr^{-1}) (Notarnicola, 2024a). These comparisons highlight that marginal snowpacks, especially those of the Greek mountains, are diminishing at some of the fastest rates observed globally.

Table 1: Mann-Kendall trends and normalized Sen's slopes for mountains with Mediterranean climates and marginal snowpacks, based on data from Notarnicola (2024a, b) and from this study (for the Greek mountains).

	Greek mountains (present study)	**Greek mountains**	**European Alps**	**Dinaric Alps**	**Apennines**	**Taurus**	**Atlas**	**Central Massif**	**Pyrenees**	**Baetic System**	**Sierra Nevada (US)**	**Snowy Mountains (AU)**
Sen's slope (% yr^{-1})	-2.4	-1.8	-1.0	-3.8	-2.7	-1.5	-2.3	-1.3	-1.1	-2.2	-0.4	3.5
p-value	**0.01**	0.37	0.07	**0.03**	**0.03**	0.4	0.14	0.49	0.09	**0.04**	0.92	0.09

The strong anticorrelation between SCA and air temperature – along with the moderate correlation with precipitation – across the ten massifs is consistent with findings from other Mediterranean mountain regions (Alonso-González et al., 2020; López-Moreno et al., 2025). These relationships indicate that temperature is the dominant control on SCA throughout the snow season, reflecting its dual influence on both atmospheric processes (e.g., the partitioning of precipitation into rain or snow) and land-surface snowpack processes, including accumulation, compaction, sublimation, and melt (Fayad et al., 2017). The role of precipitation, significant mainly in early (November-December) and late winter (February-March), aligns with the region's seasonal dynamics, during which zonal and meridional circulation patterns respectively contribute most to snow accumulation (Bartzokas et al., 2003). However, the lack of a persistent drying trend in recent decades (Fig. A8; Lagouvardos et al., 2024; Vicente-Serrano et al., 2025) suggests that declining snowfall, and therefore decreasing SCA, is primarily temperature-driven rather than the result of reduced precipitation (Abbas et al., 2024; Barnett et al., 2005; Giorgi et al., 1997; Kad et al., 2023; Li et al., 2025; Monteiro and Morin, 2023; Pepin et al., 2015, 2022; Rottler et al., 2019).

In contrast to the strong anticorrelation between SCA and temperature, the negative correlations with the NAO, AO, and AMO are generally weak and become significant only during the peak of the snow season (February-March), with small spatial variations among the massifs. The concurrent timing of the NAO and AO anticorrelations likely reflects large-scale synoptic patterns that influence the northeastern Mediterranean in late winter, particularly the formation of a blocking Central European anticyclone or the expansion of the Siberian anticyclone, and their downstream effects over the Balkans and eastern Mediterranean (Bartzokas et al., 2003; Tayanç et al., 1998). While the NAO exerts a strong influence on winter precipitation and temperature over the western Mediterranean (Lionello et al., 2006; López-Moreno et al., 2011), thereby modulating SCA in regions such as the Atlas Mountains (Marchane et al., 2016), our results indicate that this influence weakens markedly toward the eastern Mediterranean.

Although climate change is often associated with increased variability (Nordling et al., 2025; Pendergrass et al., 2017), our comparison of two 21-year subperiods (1984/1985-2004/2005 and 2004/2005-2024/2025) revealed no consistent changes in SCA variability across the ten massifs. This likely reflects the magnitude and spatial scale at which snow cover has declined over the past four decades. Furthermore, the rapid warming of the eastern Mediterranean and Greece (Lagouvardos et al., 2024), combined with the strong influence of temperature on SCA, means that even in years with exceptional snowfall, such as February 2022 (Patlakas et al., 2024), snowpack conditions remain unfavourable for persistent cover, leading to accelerated melt.

These findings are particularly relevant for marginal snowpacks in mountains with Mediterranean and Mediterranean-like climates, which are shifting towards increasingly ephemeral snow cover (López-Moreno et al., 2025; Sturm and Liston, 2021). They also carry implications for more continental mountain ranges that currently maintain seasonal snowpacks but may be transitioning toward marginal conditions. Underlined by the decreasing magnitude of positive SCA anomalies and the increasing frequency of negative ones, our results add to a growing body of evidence warning of escalating snow-drought risk in Mediterranean and global mountain regions (Avanzi et al., 2024, 2025; Baba et al., 2025; Gottlieb and Mankin, 2025; Han et al., 2025; Pokharel et al., 2024; Singh et al., 2025). Taken together, these conclusions highlight the urgent need for modernising and optimising water-resource management strategies in Greece.

4.2 snowMapper skill

snowMapper demonstrated strong skill in reconstructing a 41-year snow-cover climatology across the temperate mountains of mainland Greece. The framework provides a modular, medium-complexity solution for gap-filling spatially and temporally patchy satellite observations, using a novel modelling approach that integrates area masking, preprocessing, gap-filling, post-processing, and validation. Furthermore, the high performance of the model's PIML component - achieving high accuracy despite being trained on in situ data from outside the study area - highlights its potential for broader application in other data-sparse or unmonitored mountain regions (e.g., Pritchard, 2021). In addition to offering a standalone model for directly reconstructing snow-cover time series, snowMapper could also be used as part of more complex hydrological modelling workflows, through the use of daily high-resolution snow-cover maps for deriving boundary conditions and even calculating snow depletion curves, ultimately replacing coarser-resolution MODIS-based datasets (Tekeli et al., 2005).

The slightly lower performance of snowMapper during the transitional months of the snow season reflects a well-documented challenge in snow-cover and snow-hydrological modelling (Chereque et al., 2025; Krinner et al., 2018; Toure et al., 2018). These months are characterised by high meteorological variability (e.g., air temperatures fluctuating around 0ºC that complicate rain-snow partitioning and melt-freeze cycles) and strong pre-conditioning of land-surface conditions (e.g., above-freezing ground temperatures at the start of the snow season that produce short-lived snowpacks).

We emphasise that the careful selection of a reanalysis product is essential. Because the snow reconstruction relies on reanalysis-derived air temperature and precipitation, the regional accuracy and native spatial resolution of the chosen dataset exert a strong influence on overall model quality. These factors propagate through every stage of the workflow, from MicroMet-based downscaling and the decision-tree gap-filling algorithm to the performance of the machine learning classifier. In this study, we used ECWMF's ERA5-Land, due to its comparatively high spatial resolution. Despite this, its land mask may include mountain grid cells that overlap coastal areas, potentially introducing a warm bias for mountainous terrain on islands or narrow peninsulas. In such cases, MicroMet's lapse-rate downscaling can produce positively biased air temperatures, which then propagate through the gap-filling steps and result in earlier modelled snowmelt or, in some cases, a complete absence of snow accumulation when precipitation falls under conditions perceived as too warm for snowfall.

Future versions of snowMapper will incorporate downscaling of additional meteorological variables, including incoming shortwave radiation, relative humidity, and wind speed. These additions would allow the calculation of wet-bulb temperature, providing a more physically robust alternative to the constant T_{base} used for rain-snow partitioning. Because such variables are commonly available in widely used reanalysis products, they could improve the performance of the machine-learning classifier where corresponding in situ observations exist. Furthermore, alternative machine learning approaches, such as support vector machines or regression tree boosting, will be integrated to provide additional methods for training the classifier, other than random-forest.

5. Conclusions

Our reconstruction and analysis of 41 years of snow cover across ten Greek massifs reveal a rapid and widespread decline in SCA over the past four decades, with the most pronounced reductions occurring since the early 2000s. Sustained warming emerges as the dominant driver of this decline, reflecting its dual influence on both atmospheric processes – through its control on the fraction of precipitation falling as snow – and on snowpack processes at the surface. In contrast, precipitation correlates with SCA only during early and mid-winter, when most seasonal accumulation occurs. The generally weak relationships between SCA and the NAO, AO and AMO further indicate that the observed variability and rapid loss of snow cover are driven primarily by anthropogenic radiative forcing rather than natural modes of climate variability.

The high skill, versatility, and fully configurable architecture of snowMapper make it a valuable new tool for reconstructing daily snow-cover conditions over mountainous areas at high spatial resolution. Because it does not require local in situ data for training, we hope that the snow science community will use snowMapper to illuminate snow-cover dynamics in other mountain regions where snow is a vital water resource but where data limitations continue to constrain effective water-resource management.

Appendix A

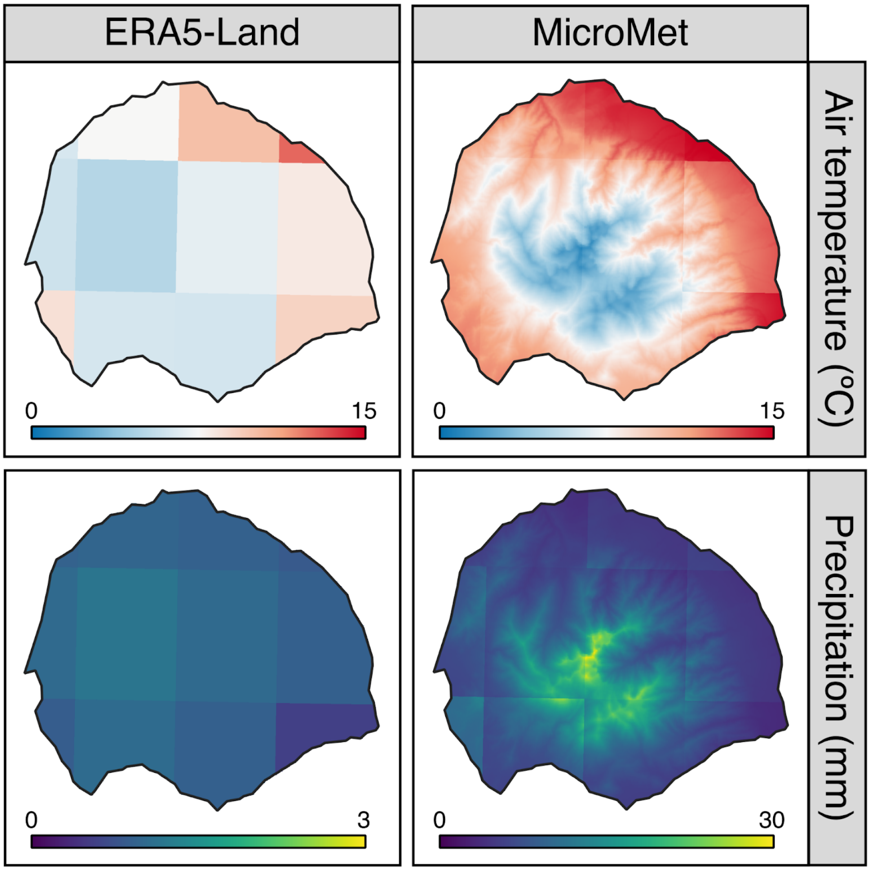

Figure A1: Example of MicroMet downscalling of ERA5-Land air temperature and precipitation to a 100 m spatial resolution (Mt. Olympus, 11 December 2022).

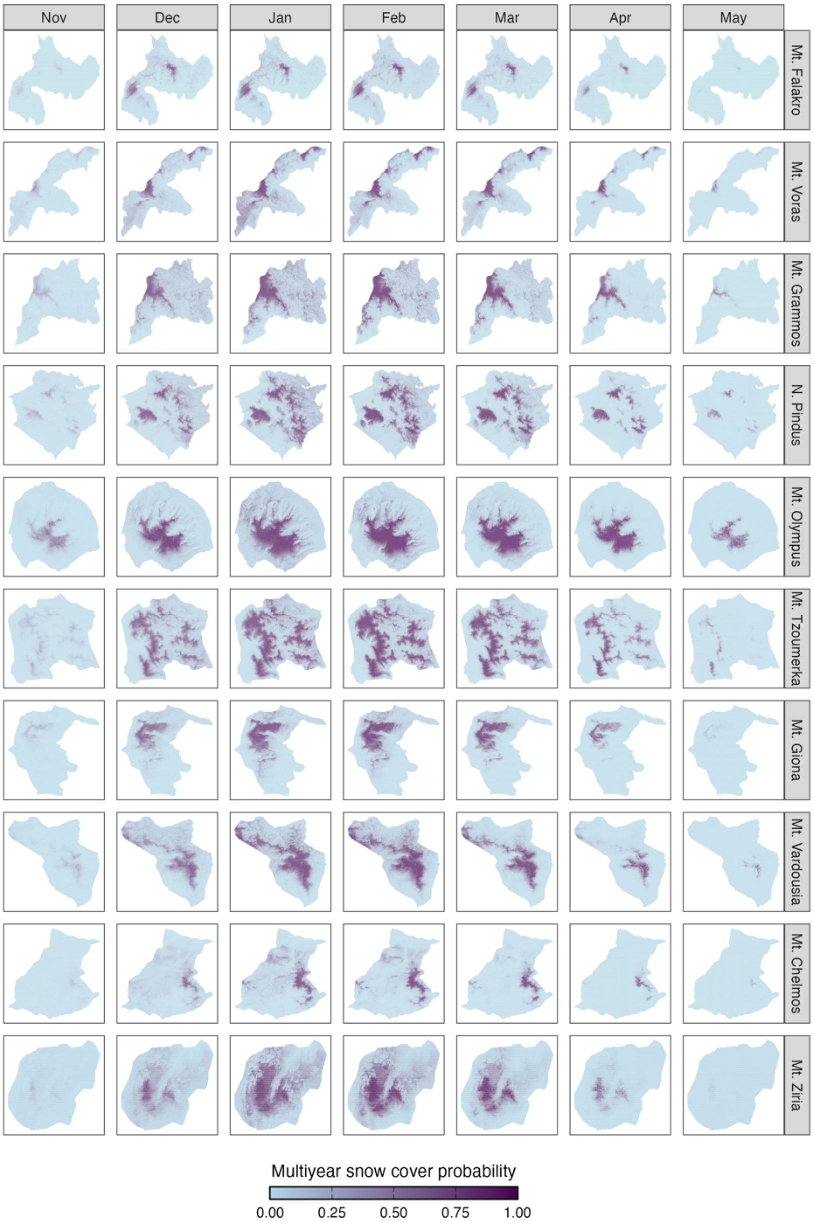

Figure A2: Monthly multiyear snow cover probabilities, calculated for the massifs of the study area (north to south) from all available Landsat & Sentinel-2 clear-sky observations between November 1984 and May 2025.

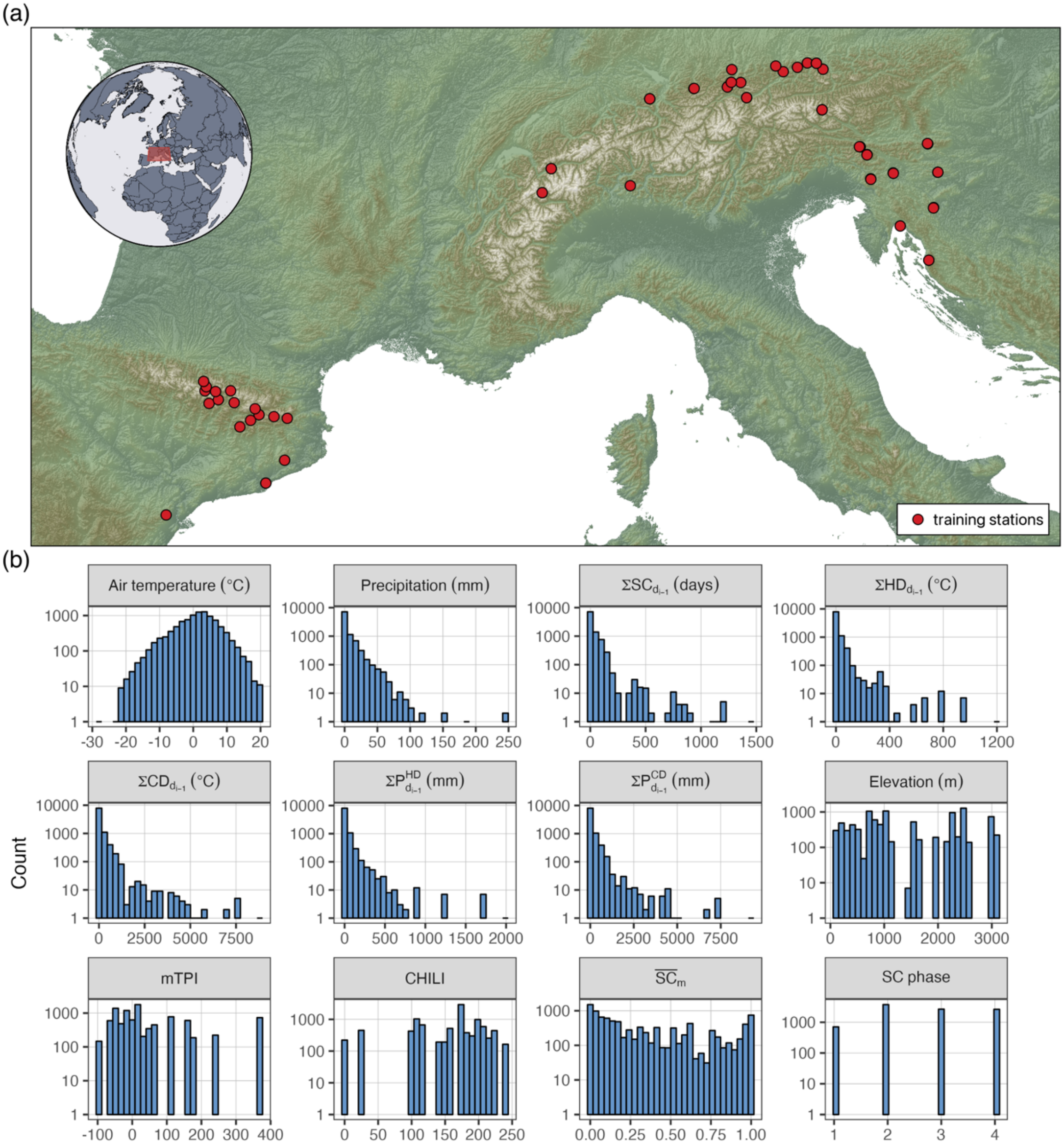

Figure A3: (a) Locations of the in situ stations (n=49) from the ECA&D network, used to train the random forest classifier. (b) Logarithmic distribution of sampled in situ data points (n=9,735) per variable. Previous day's cumulative variables are calculated through Eq. (7). Snow cover phases (Eq. 8) in the last panel are: new snow (1), snow (2), melted snow (3), and no snow (4).

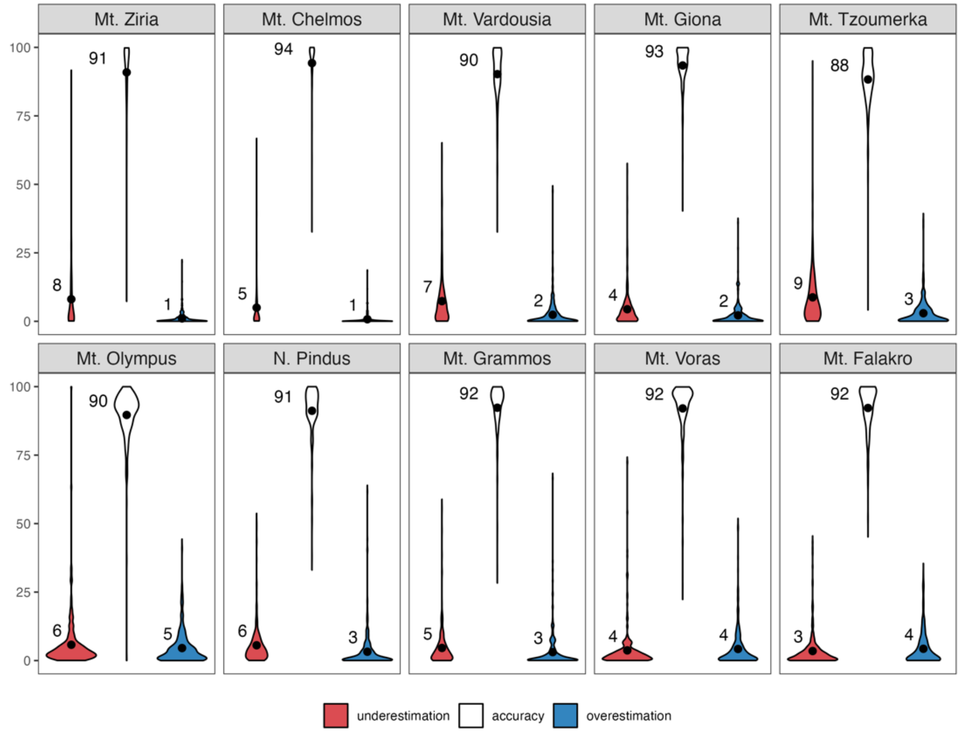

Figure A4: Violin plots of the overall model skill (i.e., accuracy, overestimation, and underestimation calculated through Eq. 11-13) for snow mapping and reconstruction for the ten massifs of the study area over the entire time-series. The black dot and associated number in each violin plot indicate the mean value of the skill metric for that massif.

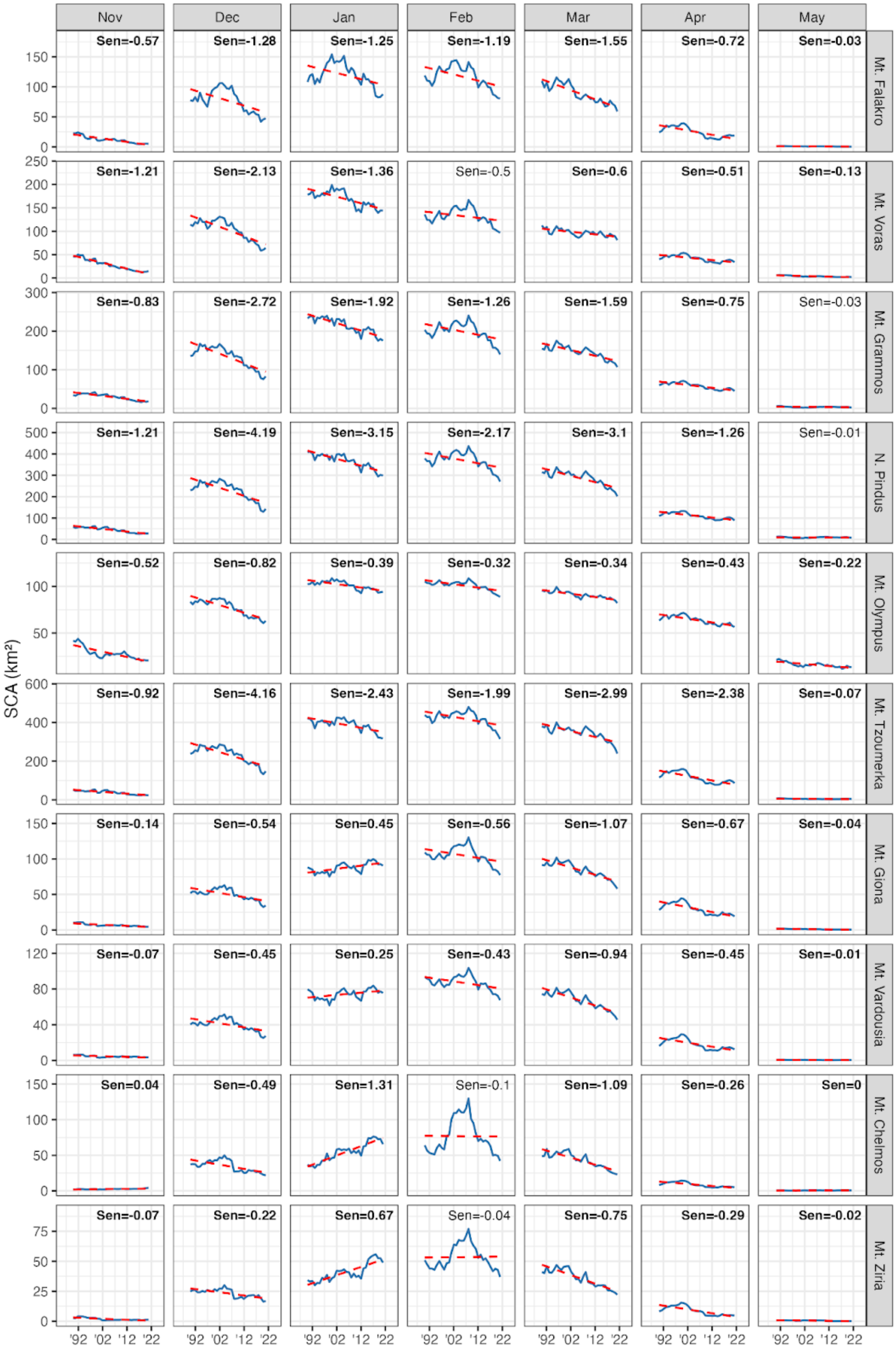

Figure A5: Monthly SCA time-series per massif, smoothed using a 10-year rolling mean. The blue line represents the monthly SCA, while the red line shows the corresponding Sen's slope (SCA loss in km^2 yr^{-1}). Bold text indicates statistically significant trends.

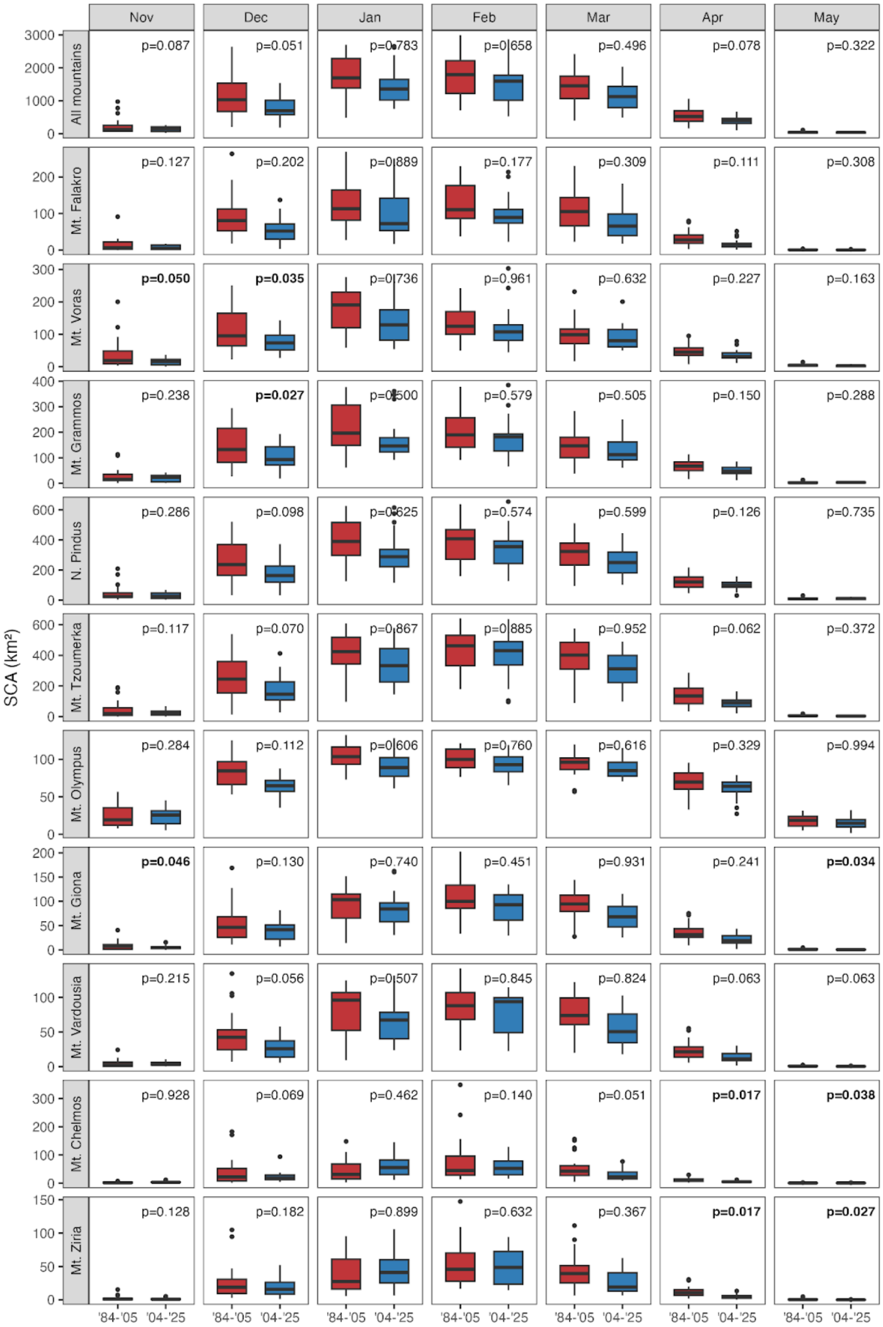

Figure A6: Monthly SCA variability per massif for the periods 1984-2005 and 2004-2025. P-values indicate the statistical significance of differences in variability between the two periods. Bold text denotes statistically significant differences.

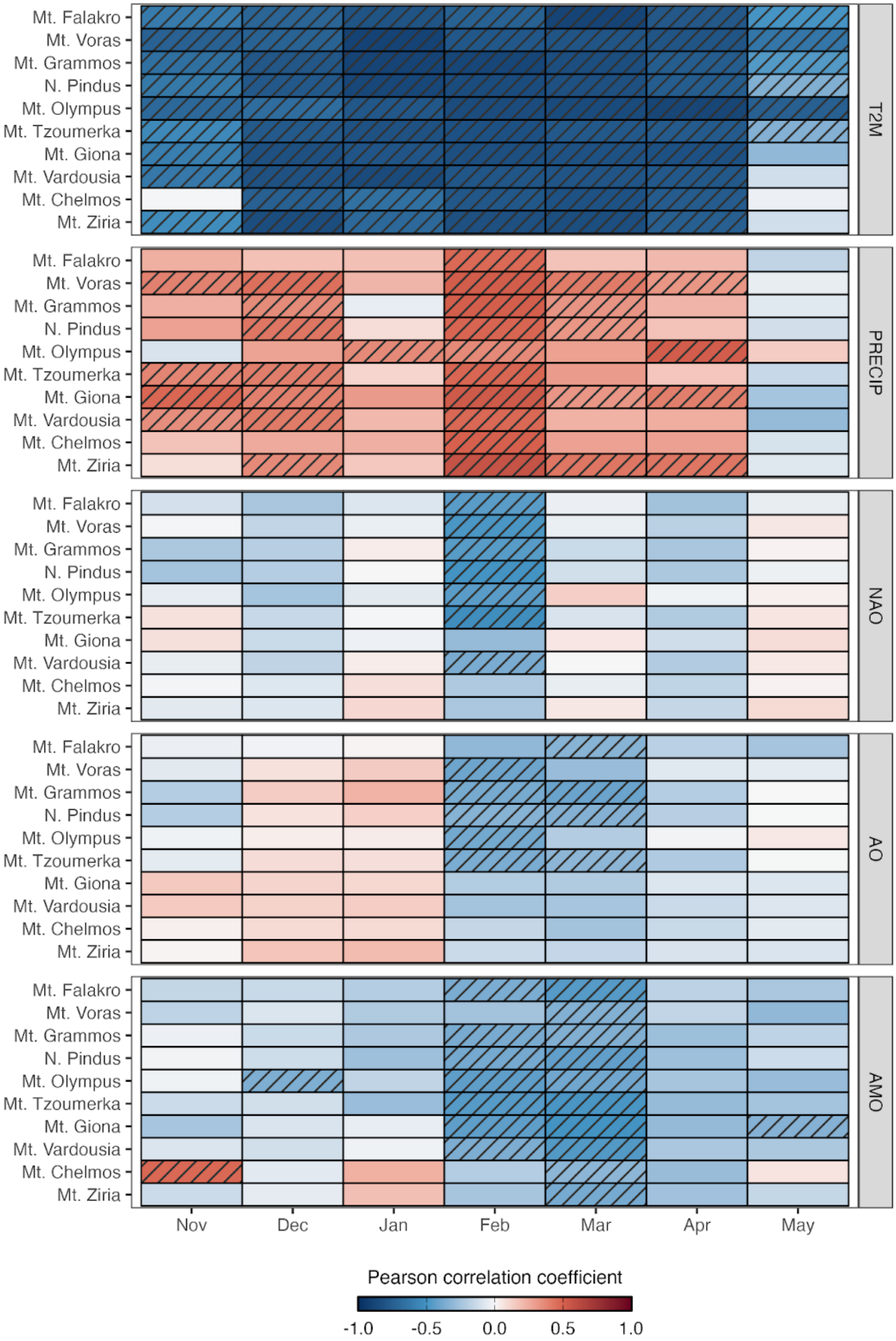

630 **Figure A7: Monthly correlations per massif between SCA and air temperature (T2M), precipitation (PRECIP), the North Atlantic Oscillation (NAO), the Arctic Oscillation (AO), and the Atlantic Multidecadal Oscillation (AMO). Hatching indicates statistically significant correlations.**

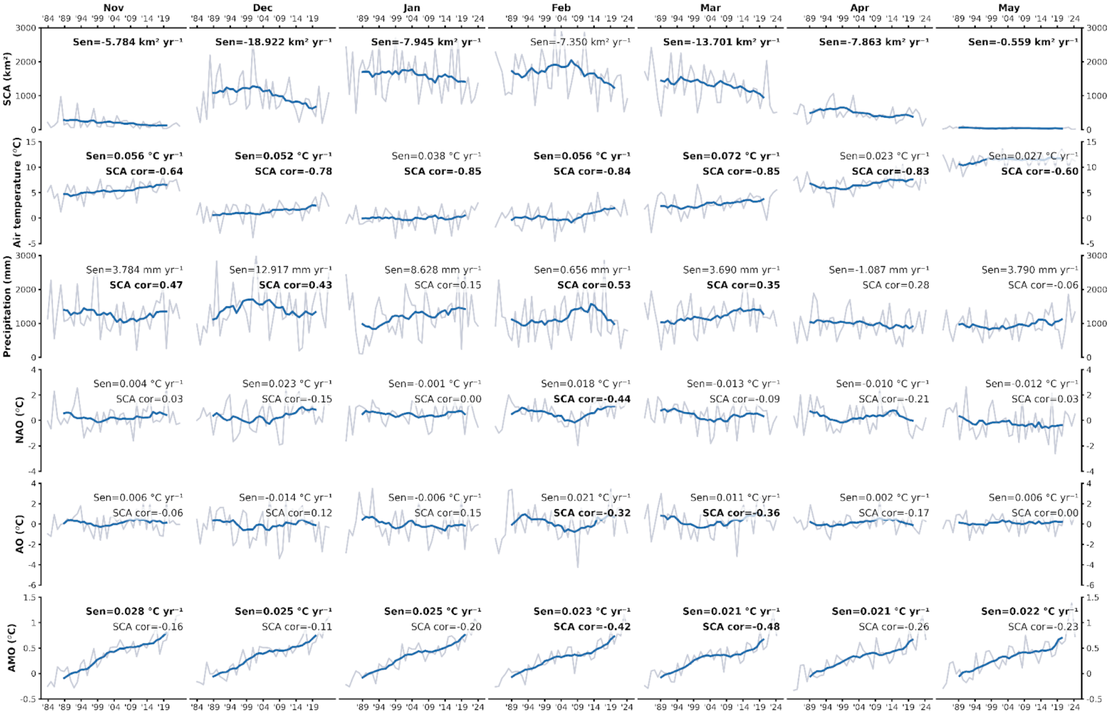

Figure A8: Monthly timeseries (grey lines), 10-year smoothed timeseries (blue lines), trends (Mann Kendall/Sen's slope), and Pearson correlations between SCA and air temperature, precipitation, the NAO, the AO, and the AMO. Bold text indicates statistically significant trends or correlations.

Code availability

The snowMapper model code and supporting notebooks are available on GitHub under the MIT license, a short and simple permissive license with conditions only requiring preservation of copyright and license notices. The download site for the model code is https://github.com/snowMapper/snowMapper (last access: 15 September 2025). The model in the presented version (v1.0.0) is available on Zenodo (https://doi.org/10.5281/zenodo.17663731, Alexopoulos et al., 2025).

Data availability

Data products generated in this work (monthly spatiotemporal FSC aggregates over ten GMBA massifs in Greece) are available for download at https://doi.org/10.5281/zenodo.19335252 (Alexopoulos et al., 2026). The GMBA Mountain Inventory v2 dataset was downloaded from https://doi.org/10.48601/earthenv-t9k2-1407 (last access: 15 September 2025). The following datasets were sourced from the Google Earth Engine Data Catalogue (https://developers.google.com/earth-engine/datasets, last access: 15 September 2025): Landsat and Sentinel-2 imagery; MODIS Fractional Snow Cover; SRTM DEM, CHILI, and mTPI; ERA5-Land. The geopotential layer for ERA5-Land, required for the calculation of geopotential height, was not available through the Google Earth Engine Data Catalogue, and was therefore downloaded directly from the Copernicus

Climate Data Store (https://cds.climate.copernicus.eu/datasets/reanalysis-era5-land?tab=overview, last access: 15 September 2025). The Tree Cover Density raster layer used for the tree mask was downloaded from the Copernicus Land Monitoring Service (https://sdi.eea.europa.eu/catalogue/copernicus/api/records/8bfbda74-7b62-4659-96dd-86600ea425a2?language=all, last access: 15 September 2025). Station temperature, precipitation, and snow depth data used for the training of the machine learning classifier were downloaded directly from the ECA&D website (https://www.ecad.eu/, last access: 15 September 2025). The NAO and AO index time-series were downloaded from National Oceanographic and Atmoshperic Administration (https://www.cpc.ncep.noaa.gov/products/precip/CWlink/daily_ao_index/teleconnections.shtml), while the AMO time-series was downloaded from the National Center for Atmospheric Research (https://climatedataguide.ucar.edu/climate-data/atlantic-multi-decadal-oscillation-amo). The MODIS-based snow cover phenology dataset over global mountain regions is made available by Notarnicola (2024a).

Author contribution

KA, ICW, HDP, and KL conceptualized the study. KA developed the methodology with contributions from all co-authors. KA and GK developed the snowMapper v1.0 software and curated the data. KA conducted the formal analysis, validation, and visualization. KA prepared the manuscript with contributions from all co-authors.

Competing interests

The authors declare that they have no conflict of interest.

Acknowledgements

We would like to thank Ujaval Gandhi & Vigna Purohit (Spatial Thoughts) for their valuable suggestions regarding Google Earth Engine ‘best practices’ during the final development stages of the snowMapper v1.0 model code. We would also like to acknowledge ESA, USGS, NSIDC, NASA, ECMWF and ECA&D, as well as Dr. Claudia Notarnicola, for making their datasets and analyses openly available, making studies like ours possible. Furthermore, we would like to acknowledge the Integration and Application Network (ian.umces.edu/media-library) for providing cost and royalty free graphics, used within Figure 2. Moreover, we would like to acknowledge Google Earth Engine for supporting the scientific community by enabling snow and climate-related research through the distribution of the above data, and the provision of free cloud storage and computational resources. Finally, we would like to thank Dr. Simon Gascoin and Mostafa Bousbaa for their time reviewing our study and for their insightful feedback on it, which helped us significantly improve the quality of this manuscript.

Financial support

KA is supported by the Bodossaki Foundation postgraduate scholarship (BDA-6898), the George & Marie Vergottis scholarship awarded via the Cambridge Trust, and the Royal Geographical Society (with the Institute of British Geographers) Postgraduate Research Award (PRA 26.24).

References

Abbas, H., Daramola, M. T., and Xu, M.: Elevation-dependent warming and possible-driving mechanisms over global highlands, Int. J. Climatol., n/a, https://doi.org/10.1002/joc.8572, 2024.

Akyurek, Z., Kuter, S., Karaman, Ç. H., and Akpınar, B.: Understanding the Snow Cover Climatology over Turkey from ERA5-Land Reanalysis Data and MODIS Snow Cover Frequency Product, Geosciences, 13, 311, https://doi.org/10.3390/geosciences13100311, 2023.

Alexopoulos, K., Willis, I., Pritchard, H., Kyros, G., Kotroni, V., and Lagouvardos, K.: snowMapper v1.0.0 (v1.0.0), Zenodo [code], https://doi.org/10.5281/zenodo.17663731, 2025.

Alexopoulos, K., Willis, I., Pritchard, H., Kyros, G., Kotroni, V., and Lagouvardos, K.: Monthly Fractional Snow Cover aggregates over the Greek mountains reconstructed with snowMapper, Zenodo [data set], https://doi.org/10.5281/zenodo.19335252, 2026.

Alonso-González, E., López-Moreno, J. I., Navarro-Serrano, F., Sanmiguel-Vallelado, A., Aznárez-Balta, M., Revuelto, J., and Ceballos, A.: Snowpack sensitivity to temperature, precipitation, and solar radiation variability over an elevational gradient in the Iberian mountains, Atmospheric Res., 243, 104973, https://doi.org/10.1016/j.atmosres.2020.104973, 2020.

Aragon, C. M. and Hill, D. F.: Changing snow water storage in natural snow reservoirs, Hydrology and Earth System Sciences, 28, 781–800, https://doi.org/10.5194/hess-28-781-2024, 2024.

Avanzi, F., Munerol, F., Milelli, M., Gabellani, S., Massari, C., Girotto, M., Cremonese, E., Galvagno, M., Bruno, G., Morra di Cella, U., Rossi, L., Altamura, M., and Ferraris, L.: Winter snow deficit was a harbinger of summer 2022 socio-hydrologic drought in the Po Basin, Italy, Commun. Earth Environ., 5, 1–12, https://doi.org/10.1038/s43247-024-01222-z, 2024.

Avanzi, F., Terzi, S., Castelli, M., Munerol, F., Andreaggi, M., Galvagno, M., Galletti, A., Maurer, T., Massari, C., Carlson, G., Girotto, M., Bertoldi, G., Cremonese, E., Gabellani, S., Cella, U. M. D., Altamura, M., Rossi, L., and Ferraris, L.: Today's snow and tomorrow's water: impacts of Mediterranean snow droughts on mountain socio-ecohydrology, https://doi.org/10.22541/au.176055865.50800695/v1, 15 October 2025.

Baba, W. M., Chehbouni, A., Ouassanouan, Y., Gascoin, S., Paganini, M., Ottavianelli, G., and Szantoi, Z.: Monitoring water crisis from space across a Mediterranean region, Sci. Rep., 15, 23262, https://doi.org/10.1038/s41598-025-06240-1, 2025.

Barella, R., Marin, C., Gianinetto, M., and Notarnicola, C.: A Novel Approach to High Resolution Snow Cover Fraction Retrieval in Mountainous Regions, in: IGARSS 2022 - 2022 IEEE International Geoscience and Remote Sensing Symposium, IGARSS 2022 - 2022 IEEE International Geoscience and Remote Sensing Symposium, 3856–3859, https://doi.org/10.1109/IGARSS46834.2022.9884177, 2022.

Barnett, T. P., Adam, J. C., and Lettenmaier, D. P.: Potential impacts of a warming climate on water availability in snow-dominated regions, Nature, 438, 303–309, https://doi.org/10.1038/nature04141, 2005.

Barrou Dumont, Z., Gascoin, S., Inglada, J., Dietz, A., Köhler, J., Lafaysse, M., Monteiro, D., Carmagnola, C., Bayle, A., Dedieu, J.-P., Hagolle, O., and Choler, P.: Trends in the annual snow melt-out day over the French Alps and Pyrenees from 38 years of high-resolution satellite data (1986–2023), The Cryosphere, 19, 2407–2429, https://doi.org/10.5194/tc-19-2407-2025, 2025.

Bartzokas, A., Lolis, C. J., and Metaxas, D. A.: A study on the intra-annual variation and the spatial distribution of precipitation amount and duration over Greece on a 10 day basis, Int. J. Climatol., 23, 207–222, https://doi.org/10.1002/joc.874, 2003.

Bayle, A., Gascoin, S., Berner, L. T., and Choler, P.: Landsat-based greening trends in alpine ecosystems are inflated by multidecadal increases in summer observations, Ecography, 2024, e07394, https://doi.org/10.1111/ecog.07394, 2024.

Belcore, E., Piras, M., and Wozniak, E.: Scecific alpine environment land cover classification methodology: Google Earth Engine processing for Serntinel-2 data, Int. Arch. Photogramm. Remote Sens. Spatial Inf. Sci., XLIII-B3-2020, 663–670, https://doi.org/10.5194/isprs-archives-XLIII-B3-2020-663-2020, 2020.

Bousbaa, M., Boudhar, A., Kinnard, C., Elyoussfi, H., Karaoui, I., Eljabiri, Y., Bouamri, H., and Chehbouni, A.: An accurate snow cover product for the Moroccan Atlas Mountains: Optimization of the MODIS NDSI index threshold and development of snow fraction estimation models, International Journal of Applied Earth Observation and Geoinformation, 129, 103851, https://doi.org/10.1016/j.jag.2024.103851, 2024.

Bousbaa, M., Htitiou, A., Boudhar, A., Eljabiri, Y., Elyoussfi, H., Bouamri, H., Ouatiki, H., and Chehbouni, A.: High-Resolution Monitoring of the Snow Cover on the Moroccan Atlas through the Spatio-Temporal Fusion of Landsat and Sentinel-2 Images, Remote Sens., 14, 5814, https://doi.org/10.3390/rs14225814, 2022.

Breiman, L.: Random Forests, Mach. Learn., 45, 5–32, https://doi.org/10.1023/A:1010933404324, 2001.

Capozzi, V., Serrapica, F., Rocco, A., Annella, C., and Budillon, G.: Historical snow measurements in the central and southern Apennine Mountains: climatology, variability, and trend, The Cryosphere, 19, 565–595, https://doi.org/10.5194/tc-19-565-2025, 2025.

Chereque, A. E., Kushner, P. J., Mudryk, L., and Derksen, C.: Determining the cause of inconsistent onset-season trends in the Northern Hemisphere snow cover extent record, Sci. Adv., 11, eadv7926, https://doi.org/10.1126/sciadv.adv7926, 2025.

Choler, P., Bayle, A., Fort, N., and Gascoin, S.: Waning snowfields have transformed into hotspots of greening within the alpine zone, Nat. Clim. Change, 1–6, https://doi.org/10.1038/s41558-024-02177-x, 2024.

Choler, P., Bonfanti, N., Reverdy, A., Bayle, A., Nicoud, B., Liger, L., Clément, J.-C., Cohard, J.-M., Corona, C., Gascoin, S., Voisin, D., and Poulenard, J.: Legacy of snow cover on alpine landscapes, Commun. Earth Environ., 6, 758, https://doi.org/10.1038/s43247-025-02702-6, 2025.

European Environment Agency: Tree Cover Density 2015 (raster 20 m), Europe, 3-yearly, Mar. 2018, https://doi.org/10.2909/8bfbda74-7b62-4659-96dd-86600ea425a2, 2018.

Farr, T. G., Rosen, P. A., Caro, E., Crippen, R., Duren, R., Hensley, S., Kobrick, M., Paller, M., Rodriguez, E., Roth, L., Seal, D., Shaffer, S., Shimada, J., Umland, J., Werner, M., Oskin, M., Burbank, D., and Alsdorf, D.: The Shuttle Radar Topography Mission, Rev. Geophys., 45, https://doi.org/10.1029/2005RG000183, 2007.

Faranda, D.: An attempt to explain recent changes in European snowfall extremes, Weather and Climate Dynamics, 1, 445–458, https://doi.org/10.5194/wcd-1-445-2020, 2020.

Fayad, A., Gascoin, S., Faour, G., López-Moreno, J. I., Drapeau, L., Page, M. L., and Escadafal, R.: Snow hydrology in Mediterranean mountain regions: A review, J. Hydrol., 551, 374–396, https://doi.org/10.1016/j.jhydrol.2017.05.063, 2017.

Fiddes, J. and Gruber, S.: TopoSCALE v.1.0: downscaling gridded climate data in complex terrain, Geosci. Model Dev., 7, 387–405, https://doi.org/10.5194/gmd-7-387-2014, 2014.

Foga, S., Scaramuzza, P. L., Guo, S., Zhu, Z., Dilley, R. D., Beckmann, T., Schmidt, G. L., Dwyer, J. L., Joseph Hughes, M., and Laue, B.: Cloud detection algorithm comparison and validation for operational Landsat data products, Remote Sens. Environ., 194, 379–390, https://doi.org/10.1016/j.rse.2017.03.026, 2017.

Gafurov, A. and Bárdossy, A.: Cloud removal methodology from MODIS snow cover product, Hydrol. Earth Syst. Sci., 13, 1361–1373, https://doi.org/10.5194/hess-13-1361-2009, 2009.

García-Ruiz, J. M., López-Moreno, J. I., Vicente-Serrano, S. M., Lasanta–Martínez, T., and Beguería, S.: Mediterranean water resources in a global change scenario, Earth-Sci. Rev., 105, 121–139, https://doi.org/10.1016/j.earscirev.2011.01.006, 2011.

Gascoin, S., Hagolle, O., Huc, M., Jarlan, L., Dejoux, J.-F., Szczypta, C., Marti, R., and Sánchez, R.: A snow cover climatology for the Pyrenees from MODIS snow products, Hydrol. Earth Syst. Sci., 19, 2337–2351, https://doi.org/10.5194/hess-19-2337-2015, 2015.

Gascoin, S., Grizonnet, M., Bouchet, M., Salgues, G., and Hagolle, O.: Theia Snow collection: high-resolution operational snow cover maps from Sentinel-2 and Landsat-8 data, Earth Syst. Sci. Data, 11, 493–514, https://doi.org/10.5194/essd-11-493-2019, 2019.

Gascoin, S., Monteiro, D., and Morin, S.: Reanalysis-based contextualization of real-time snow cover monitoring from space, Environ. Res. Lett., 17, 114044, https://doi.org/10.1088/1748-9326/ac9e6a, 2022.

Gascoin, S., Luojus, K., Nagler, T., Lievens, H., Masiokas, M., Jonas, T., Zheng, Z., and De Rosnay, P.: Remote sensing of mountain snow from space: status and recommendations, Front. Earth Sci., 12, https://doi.org/10.3389/feart.2024.1381323, 2024.

Giorgi, F.: Climate change hot-spots, Geophys. Res. Lett., 33, https://doi.org/10.1029/2006GL025734, 2006.

Giorgi, F., Hurrell, J. W., Marinucci, M. R., and Beniston, M.: Elevation Dependency of the Surface Climate Change Signal: A Model Study, J. Clim., 10, 288–296, https://doi.org/10.1175/1520-0442(1997)010%253C0288:EDOTSC%253E2.0.CO;2, 1997.

Gorelick, N., Hancher, M., Dixon, M., Ilyushchenko, S., Thau, D., and Moore, R.: Google Earth Engine: Planetary-scale geospatial analysis for everyone, Remote Sens. Environ., 202, 18–27, https://doi.org/10.1016/j.rse.2017.06.031, 2017.

Gottlieb, A. R. and Mankin, J. S.: Evidence of human influence on Northern Hemisphere snow loss, Nature, 625, 293–300, https://doi.org/10.1038/s41586-023-06794-y, 2024.

Gottlieb, A. R. and Mankin, J. S.: Subseasonal Temperature Variability Drives Nonlinear Snow Loss With Warming, Water Resour. Res., 61, e2024WR039724, https://doi.org/10.1029/2024WR039724, 2025.

Hall, D. K. and Riggs, G. A.: MODIS/Terra Snow Cover Daily L3 Global 500m SIN Grid, Version 6, https://doi.org/10.5067/MODIS/MOD10A1.006, 2015.

Hamed, K. H. and Ramachandra Rao, A.: A modified Mann-Kendall trend test for autocorrelated data, Journal of Hydrology, 204, 182–196, https://doi.org/10.1016/S0022-1694(97)00125-X, 1998.

Han, J., Yang, Y., Xiong, H., Guo, Y., Li, C., and Liu, Z.: Accelerated propagation from meteorological to hydrological drought under diminishing snow, Environ. Res. Lett., 20, 054076, https://doi.org/10.1088/1748-9326/adccdc, 2025.

Härer, S., Bernhardt, M., Siebers, M., and Schulz, K.: On the need for a time- and location-dependent estimation of the NDSI threshold value for reducing existing uncertainties in snow cover maps at different scales, The Cryosphere, 12, 1629–1642, https://doi.org/10.5194/tc-12-1629-2018, 2018.

Kad, P., Ha, K.-J., Lee, S.-S., and Chu, J.-E.: Projected Changes in Mountain Precipitation Under CO2-Induced Warmer Climate, Earths Future, 11, e2023EF003886, https://doi.org/10.1029/2023EF003886, 2023.

Klein Tank, A. M. G., Wijngaard, J. B., Können, G. P., Böhm, R., Demarée, G., Gocheva, A., Mileta, M., Pashiardis, S., Hejkrlik, L., Kern-Hansen, C., Heino, R., Bessemoulin, P., Müller-Westermeier, G., Tzanakou, M., Szalai, S., Pálsdóttir, T., Fitzgerald, D., Rubin, S., Capaldo, M., Maugeri, M., Leitass, A., Bukantis, A., Aberfeld, R., van Engelen, A. F. V., Forland, E., Mietus, M., Coelho, F., Mares, C., Razuvaev, V., Nieplova, E., Cegnar, T., Antonio López, J., Dahlström, B., Moberg, A., Kirchhofer, W., Ceylan, A., Pachaliuk, O., Alexander, L. V., and Petrovic, P.: Daily dataset of 20th-century surface air temperature and precipitation series for the European Climate Assessment, Int. J. Climatol., 22, 1441–1453, https://doi.org/10.1002/joc.773, 2002.

Kashinath, K., Mustafa, M., Albert, A., Wu, J.-L., Jiang, C., Esmaeilzadeh, S., Azizzadenesheli, K., Wang, R., Chattopadhyay, A., Singh, A., Manepalli, A., Chirila, D., Yu, R., Walters, R., White, B., Xiao, H., Tchelepi, H. A., Marcus, P., Anandkumar, A., Hassanzadeh, P., and Prabhat: Physics-informed machine learning: case studies for weather and climate modelling, Philos Trans A Math Phys Eng Sci, 379, 20200093, https://doi.org/10.1098/rsta.2020.0093, 2021.

Koehler, J., Bauer, A., Dietz, A. J., and Kuenzer, C.: Towards Forecasting Future Snow Cover Dynamics in the European Alps—The Potential of Long Optical Remote-Sensing Time Series, Remote Sens., 14, 4461, https://doi.org/10.3390/rs14184461, 2022.

Kollert, A., Mayr, A., Dullinger, S., Hülber, K., Moser, D., Lhermitte, S., Gascoin, S., and Rutzinger, M.: Downscaling MODIS NDSI to Sentinel-2 fractional snow cover by random forest regression, Remote Sens. Lett., 15, 363–372, https://doi.org/10.1080/2150704X.2024.2327084, 2024.

Kotroni, V., Bezes, A., Dafis, S., Founda, D., Galanaki, E., Giannaros, C., Giannaros, T., Karagiannidis, A., Koletsis, I., Kyros, G., Lagouvardos, K., Papagiannaki, K., and Papavasileiou, G.: Long-Term Statistical Analysis of Severe Weather and Climate Events in Greece, Atmosphere, 16, 105, https://doi.org/10.3390/atmos16010105, 2025.

Krinner, G., Derksen, C., Essery, R., Flanner, M., Hagemann, S., Clark, M., Hall, A., Rott, H., Brutel-Vuilmet, C., Kim, H., Ménard, C. B., Mudryk, L., Thackeray, C., Wang, L., Arduini, G., Balsamo, G., Bartlett, P., Boike, J., Boone, A., Chéruy, F., Colin, J., Cuntz, M., Dai, Y., Decharme, B., Derry, J., Ducharne, A., Dutra, E., Fang, X., Fierz, C., Ghattas, J., Gusev, Y., Haverd, V., Kontu, A., Lafaysse, M., Law, R., Lawrence, D., Li, W., Marke, T., Marks, D., Ménégoz, M., Nasonova, O., Nitta, T., Niwano, M., Pomeroy, J., Raleigh, M. S., Schaedler, G., Semenov, V., Smirnova, T. G., Stacke, T., Strasser, U., Svenson, S., Turkov, D., Wang, T., Wever, N., Yuan, H., Zhou, W., and Zhu, D.: ESM-SnowMIP: assessing snow models and quantifying snow-related climate feedbacks, Geosci. Model Dev., 11, 5027–5049, https://doi.org/10.5194/gmd-11-5027-2018, 2018.

Hu, J. M. and Shean, D.: Improving Mountain Snow and Land Cover Mapping Using Very-High-Resolution (VHR) Optical Satellite Images and Random Forest Machine Learning Models, Remote Sensing, 14, 4227, https://doi.org/10.3390/rs14174227, 2022.

Kunkel, K. E.: Simple Procedures for Extrapolation of Humidity Variables in the Mountainous Western United States, J. Clim., 2, 656–669, https://doi.org/10.1175/1520-0442(1989)002%253C0656:SPFEOH%253E2.0.CO;2, 1989.

Lagouvardos, K., Dafis, S., Kotroni, V., Kyros, G., and Giannaros, C.: Exploring Recent (1991–2020) Trends of Essential Climate Variables in Greece, Atmosphere, 15, 1104, https://doi.org/10.3390/atmos15091104, 2024.

Li, Y.-P., Chen, Y.-N., Sun, F., Li, Z., Fang, G.-H., Wang, F., Zhang, X.-Q., and Li, B.-F.: Contrasting trends of extreme rainfall and snowfall in the Northern Hemisphere, Advances in Climate Change Research, https://doi.org/10.1016/j.accre.2025.09.002, 2025.

Lionello, P., Malanotte-Rizzoli, P., Boscolo, R., Alpert, P., Artale, V., Li, L., Luterbacher, J., May, W., Trigo, R., Tsimplis, M., Ulbrich, U., and Xoplaki, E.: The Mediterranean climate: An overview of the main characteristics and issues, in: Developments in Earth and Environmental Sciences, vol. 4, edited by: Lionello, P., Malanotte-Rizzoli, P., and Boscolo, R., Elsevier, 1–26, https://doi.org/10.1016/S1571-9197(06)80003-0, 2006.

Liston, G. E. and Elder, K.: A Distributed Snow-Evolution Modeling System (SnowModel), Journal of Hydrometeorology, 7, 1259–1276, https://doi.org/10.1175/JHM548.1, 2006a.

Liston, G. E. and Elder, K.: A Meteorological Distribution System for High-Resolution Terrestrial Modeling (MicroMet), Journal of Hydrometeorology, 7, 217–234, https://doi.org/10.1175/JHM486.1, 2006b.

López-Moreno, J. I., Vicente-Serrano, S. M., Morán-Tejeda, E., Lorenzo-Lacruz, J., Kenawy, A., and Beniston, M.: Effects of the North Atlantic Oscillation (NAO) on combined temperature and precipitation winter modes in the Mediterranean mountains: Observed relationships and projections for the 21st century, Glob. Planet. Change, 77, 62–76, https://doi.org/10.1016/j.gloplacha.2011.03.003, 2011.

López-Moreno, J. I., Gascoin, S., Herrero, J., Sproles, E. A., Pons, M., Alonso-González, E., Hanich, L., Boudhar, A., Musselman, K. N., Molotch, N. P., Sickman, J., and Pomeroy, J.: Different sensitivities of snowpacks to warming in Mediterranean climate mountain areas, Environ. Res. Lett., 12, 074006, https://doi.org/10.1088/1748-9326/aa70cb, 2017.

López-Moreno, J. I., Callow, N., McGowan, H., Webb, R., Schwartz, A., Bilish, S., Revuelto, J., Gascoin, S., Deschamps-Berger, C., and Alonso-González, E.: Marginal snowpacks: The basis for a global definition and existing research needs, Earth-Sci. Rev., 252, 104751, https://doi.org/10.1016/j.earscirev.2024.104751, 2024.

López-Moreno, J. I., Deschamps-Berger, C., Revuelto, J. E. S. Ú. S., Alonso-González, E., Rojas-Heredia, F., and Callow, N.: The response of marginal snowpacks to climate warming, Adv. Clim. Change Res., https://doi.org/10.1016/j.accre.2025.04.014, 2025.

Loukas, A., Mylopoulos, N., and Vasiliades, L.: A Modeling System for the Evaluation of Water Resources Management Strategies in Thessaly, Greece, Water Resour. Manag., 21, 1673–1702, https://doi.org/10.1007/s11269-006-9120-5, 2007.

Mahanthege, S., Kleiber, W., Rittger, K., Rajagopalan, B., Brodzik, M. J., and Bair, E.: A Spatially-Distributed Machine Learning Approach for Fractional Snow Covered Area Estimation, Water Resour. Res., 60, e2023WR036162, https://doi.org/10.1029/2023WR036162, 2024.

Maharjan, S., Li, W., Thomas, R., Fazli, S., Ansari, A., Morgan, H., Elgendy, A., Allali, M., and El-Askary, H.: Physics-informed deep learning reveals climate-driven snowpack decline and threatens ecological water availability in a Californian snow-fed catchment, Ecological Informatics, 92, 103526, https://doi.org/10.1016/j.ecoinf.2025.103526, 2025.

Masloumidis, I., Dafis, S., Kyros, G., Lagouvardos, K., and Kotroni, V.: Snow Cover and Depth Climatology and Trends in Greece, Climate, 13, 34, https://doi.org/10.3390/cli13020034, 2025.

Matiu, M. and Hanzer, F.: Bias adjustment and downscaling of snow cover fraction projections from regional climate models using remote sensing for the European Alps, Hydrol. Earth Syst. Sci., 26, 3037–3054, https://doi.org/10.5194/hess-26-3037-2022, 2022.

Matiu, M., Crespi, A., Bertoldi, G., Carmagnola, C. M., Marty, C., Morin, S., Schöner, W., Cat Berro, D., Chiogna, G., De Gregorio, L., Kotlarski, S., Majone, B., Resch, G., Terzago, S., Valt, M., Beozzo, W., Cianfarra, P., Gouttevin, I., Marcolini, G., Notarnicola, C., Petitta, M., Scherrer, S. C., Strasser, U., Winkler, M., Zebisch, M., Cicogna, A., Cremonini, R., Debernardi, A., Faletto, M., Gaddo, M., Giovannini, L., Mercalli, L., Soubeyroux, J.-M., Sušnik, A., Trenti, A., Urbani, S., and Weilguni, V.: Observed snow depth trends in the European Alps: 1971 to 2019, The Cryosphere, 15, 1343–1382, https://doi.org/10.5194/tc-15-1343-2021, 2021.

Meng, C., Griesemer, S., Cao, D., Seo, S., and Liu, Y.: When physics meets machine learning: a survey of physics-informed machine learning, Mach. Learn. Comput. Sci. Eng, 1, 20, https://doi.org/10.1007/s44379-025-00016-0, 2025.

Moazzam, M. F. U., Rahman, G., Lee, B. G., and Ansari, N. A.: Trend of snow cover under the influence of climate change using Google Earth Engine platform: A case study of Astore (Western Himalayas) and Shigar (Karakoram region), Front. Environ. Sci., 10, 2022.

Monteiro, D. and Morin, S.: Multi-decadal analysis of past winter temperature, precipitation and snow cover data in the European Alps from reanalyses, climate models and observational datasets, The Cryosphere, 17, 3617–3660, https://doi.org/10.5194/tc-17-3617-2023, 2023.

Muhuri, A., Gascoin, S., Menzel, L., Kostadinov, T. S., Harpold, A. A., Sanmiguel-Vallelado, A., and López-Moreno, J. I.: Performance Assessment of Optical Satellite-Based Operational Snow Cover Monitoring Algorithms in Forested Landscapes, IEEE J. Sel. Top. Appl. Earth Obs. Remote Sens., 14, 7159–7178, https://doi.org/10.1109/JSTARS.2021.3089655, 2021.

Muñoz-Sabater, J., Dutra, E., Agustí-Panareda, A., Albergel, C., Arduini, G., Balsamo, G., Boussetta, S., Choulga, M., Harrigan, S., Hersbach, H., Martens, B., Miralles, D. G., Piles, M., Rodríguez-Fernández, N. J., Zsoter, E., Buontempo, C., and Thépaut, J.-N.: ERA5-Land: a state-of-the-art global reanalysis dataset for land applications, Earth Syst. Sci. Data, 13, 4349–4383, https://doi.org/10.5194/essd-13-4349-2021, 2021.

Nordling, K., Fahrenbach, N. L. S., and Samset, B. H.: Climate variability can outweigh the influence of climate mean changes for extreme precipitation under global warming, Atmospheric Chem. Phys., 25, 1659–1684, https://doi.org/10.5194/acp-25-1659-2025, 2025.

Notarnicola, C.: Hotspots of snow cover changes in global mountain regions over 2000–2018, Remote Sens. Environ., 243, 111781, https://doi.org/10.1016/j.rse.2020.111781, 2020.

Notarnicola, C.: Global mountain snow cover phenology from MODIS/Terra imagery, Zenodo [data set], https://doi:10.48784/1zvv-nw59, 2024a

Notarnicola, C.: Snow cover phenology dataset over global mountain regions from 2000 to 2023, Data Brief, 56, 110860, https://doi.org/10.1016/j.dib.2024.110860, 2024b.

Pan, F., Jiang, L., Wang, G., Pan, J., Huang, J., Zhang, C., Cui, H., Yang, J., Zheng, Z., Wu, S., and Shi, J.: MODIS daily cloud-gap-filled fractional snow cover dataset of the Asian Water Tower region (2000-2022), Earth Syst. Sci. Data, 16, 2501–2523, https://doi.org/10.5194/essd-16-2501-2024, 2024.

Parajka, J. and Blöschl, G.: Spatio-temporal combination of MODIS images – potential for snow cover mapping, Water Resour. Res., 44, https://doi.org/10.1029/2007WR006204, 2008.

Pasquarella, V. J., Brown, C. F., Czerwinski, W., and Rucklidge, W. J.: Comprehensive Quality Assessment of Optical Satellite Imagery Using Weakly Supervised Video Learning, Proceedings of the IEEE/CVF Conference on Computer Vision and Pattern Recognition, 2125–2135, 2023.

Patlakas, P., Chaniotis, I., Hatzaki, M., Kouroutzoglou, J., and Flocas, H. A.: The eastern Mediterranean extreme snowfall of January 2022: synoptic analysis and impact of sea-surface temperature, Weather, 79, 25–33, https://doi.org/10.1002/wea.4397, 2024.

Pekel, J.-F., Cottam, A., Gorelick, N., and Belward, A. S.: High-resolution mapping of global surface water and its long-term changes, Nature, 540, 418–422, https://doi.org/10.1038/nature20584, 2016.

Pendergrass, A. G., Knutti, R., Lehner, F., Deser, C., and Sanderson, B. M.: Precipitation variability increases in a warmer climate, Sci. Rep., 7, 17966, https://doi.org/10.1038/s41598-017-17966-y, 2017.

Pepin, N., Bradley, R. S., Diaz, H. F., Baraer, M., Caceres, E. B., Forsythe, N., Fowler, H., Greenwood, G., Hashmi, M. Z., Liu, X. D., Miller, J. R., Ning, L., Ohmura, A., Palazzi, E., Rangwala, I., Schöner, W., Severskiy, I., Shahgedanova, M., Wang, M. B., Williamson, S. N., Yang, D. Q., and Mountain Research Initiative EDW Working Group: Elevation-dependent warming in mountain regions of the world, Nat. Clim. Change, 5, 424–430, https://doi.org/10.1038/nclimate2563, 2015.

Pepin, N. C., Arnone, E., Gobiet, A., Haslinger, K., Kotlarski, S., Notarnicola, C., Palazzi, E., Seibert, P., Serafin, S., Schöner, W., Terzago, S., Thornton, J. M., Vuille, M., and Adler, C.: Climate Changes and Their Elevational Patterns in the Mountains of the World, Rev. Geophys., 60, e2020RG000730, https://doi.org/10.1029/2020RG000730, 2022.

Pokharel, B., Jagannathan, K. A., Wang, S.-Y. S., Jones, A., LaPlante, M. D., Buddhavarapu, S., Borhara, K., Ulrich, P., Leung, L.-Y. R., Eklund, J., Hasenyager, C., Serago, J., Prairie, J. R., Kaatz, L., Winchell, T., and Kugel, F.: Can we rely on drought-ending “miracles” in the Colorado River Basin?, JAWRA J. Am. Water Resour. Assoc., 60, 813–824, https://doi.org/10.1111/1752-1688.13204, 2024.

Poussin, C., Timoner, P., Chatenoux, B., Giuliani, G., and Peduzzi, P.: Improved Landsat-based snow cover mapping accuracy using a spatiotemporal NDSI and generalized linear mixed model, Science of Remote Sensing, 7, 100078, https://doi.org/10.1016/j.srs.2023.100078, 2023.

Poussin, C., Peduzzi, P., and Giuliani, G.: Snow Observation from Space: An approach to improving snow cover detection using four decades of Landsat and Sentinel-2 imageries across Switzerland, Sci. Remote Sens., 100182, https://doi.org/10.1016/j.srs.2024.100182, 2024.

Pritchard, H. D.: Global Data Gaps in Our Knowledge of the Terrestrial Cryosphere, Front. Clim., 3, 2021.

Revuelto, J., Alonso-González, E., Gascoin, S., Rodríguez-López, G., and López-Moreno, J. I.: Spatial Downscaling of MODIS Snow Cover Observations Using Sentinel-2 Snow Products, Remote Sens., 13, 4513, https://doi.org/10.3390/rs13224513, 2021.

Rottler, E., Kormann, C., Francke, T., and Bronstert, A.: Elevation-dependent warming in the Swiss Alps 1981–2017: Features, forcings and feedbacks, Int. J. Climatol., 39, 2556–2568, https://doi.org/10.1002/joc.5970, 2019.

Rumpf, S. B., Gravey, M., Brönnimann, O., Luoto, M., Cianfrani, C., Mariethoz, G., and Guisan, A.: From white to green: Snow cover loss and increased vegetation productivity in the European Alps, Science, 376, 1119–1122, https://doi.org/10.1126/science.abn6697, 2022.

Sadeghi, M., Asakereh, H., and Darand, M.: Climatological Analysis of Variability in Snow Cover Features Across Iran During 1981–2022, Int. J. Climatol., 45, e8780, https://doi.org/10.1002/joc.8780, 2025.

Sebbar, B., Khabba, S., Merlin, O., Simonneaux, V., Hachimi, C. E., Kharrou, M. H., and Chehbouni, A.: Machine-Learning-Based Downscaling of Hourly ERA5-Land Air Temperature over Mountainous Regions, Atmosphere, 14, 610, https://doi.org/10.3390/atmos14040610, 2023.

Shea, J. M., Whitfield, P. H., Fang, X., and Pomeroy, J. W.: The Role of Basin Geometry in Mountain Snowpack Responses to Climate Change, Front. Water, 3, https://doi.org/10.3389/frwa.2021.604275, 2021.

Shen, Y., Wang, X., Zhu, R., Che, T., and Hao, X.: A Downscaling Algorithm for Snow Cover Extent Over the Tibetan Plateau Based on a Similar Conditional Probability and Otsu’s Method, IEEE Trans. Geosci. Remote Sens., 63, 1–14, https://doi.org/10.1109/TGRS.2025.3543433, 2025.

Sheykhmousa, M., Mahdianpari, M., Ghanbari, H., Mohammadimanesh, F., Ghamisi, P., and Homayouni, S.: Support Vector Machine Versus Random Forest for Remote Sensing Image Classification: A Meta-Analysis and Systematic Review, IEEE Journal of Selected Topics in Applied Earth Observations and Remote Sensing, 13, 6308–6325, https://doi.org/10.1109/JSTARS.2020.3026724, 2020.

Singh, H., Varade, D., and Gupta, V.: Intensified occurrences of snow droughts are related to the snow cover dynamics in the Hindu Kush Himalayas, Sci. Rep., 15, 36101, https://doi.org/10.1038/s41598-025-21257-2, 2025.

Snethlage, M. A., Geschke, J., Ranipeta, A., Jetz, W., Yoccoz, N. G., Körner, C., Spehn, E. M., Fischer, M., and Urbach, D.: A hierarchical inventory of the world’s mountains for global comparative mountain science, Sci. Data, 9, 149, https://doi.org/10.1038/s41597-022-01256-y, 2022a.

Snethlage, M. A., Geschke, J., Spehn, E. M., Ranipeta, A., Yoccoz, N. G., Körner, Ch., Jetz, W., Fischer, M., and Urbach, D.: GMBA Mountain Inventory v2 (2), https://doi.org/10.48601/earthenv-t9k2-1407, 2022b.

Sturm, M. and Liston, G. E.: Revisiting the Global Seasonal Snow Classification: An Updated Dataset for Earth System Applications, J. Hydrometeorol., 22, 2917–2938, https://doi.org/10.1175/JHM-D-21-0070.1, 2021.

Tayanç, M., Karaca, M., and Dalfes, H. N.: March 1987 Cyclone (Blizzard) over the Eastern Mediterranean and Balkan Region Associated with Blocking, Mon. Weather Rev., 126, 3036–3047, https://doi.org/10.1175/1520-0493(1998)126%253C3036:MCBOTE%253E2.0.CO;2, 1998.

Tekeli, A. E., Akyürek, Z., Arda Şorman, A., Şensoy, A., and Ünal Şorman, A.: Using MODIS snow cover maps in modeling snowmelt runoff process in the eastern part of Turkey, Remote Sensing of Environment, 97, 216–230, https://doi.org/10.1016/j.rse.2005.03.013, 2005.

Theobald, D. M., Harrison-Atlas, D., Monahan, W. B., and Albano, C. M.: Ecologically-Relevant Maps of Landforms and Physiographic Diversity for Climate Adaptation Planning, PLOS ONE, 10, e0143619, https://doi.org/10.1371/journal.pone.0143619, 2015.

Thornton, P. E., Running, S. W., and White, M. A.: Generating surfaces of daily meteorological variables over large regions of complex terrain, J. Hydrol., 190, 214–251, https://doi.org/10.1016/S0022-1694(96)03128-9, 1997.

Toure, A. M., Luojus, K., Rodell, M., Beaudoing, H., and Getirana, A.: Evaluation of Simulated Snow and Snowmelt Timing in the Community Land Model Using Satellite-Based Products and Streamflow Observations, J. Adv. Model. Earth Syst., 10, 2933–2951, https://doi.org/10.1029/2018MS001389, 2018.

Trancoso, R., Syktus, J., Allan, R. P., Croke, J., Hoegh-Guldberg, O., and Chadwick, R.: Significantly wetter or drier future conditions for one to two thirds of the world's population, Nat. Commun., 15, 483, https://doi.org/10.1038/s41467-023-44513-3, 2024.

Trenberth, K., Zhang, R., and National Center for Atmospheric Research Staff (Eds): The Climate Data Guide: Atlantic Multi-decadal Oscillation (AMO) and Atlantic Multidecadal Variability (AMV), 2025.

Tringa, E., Tolika, K., Anagnostopoulou, C., and Kostopoulou, E.: A Climatological and Synoptic Analysis of Winter Cold Spells over the Balkan Peninsula, Atmosphere, 13, https://doi.org/10.3390/atmos13111851, 2022.

Vicente-Serrano, S. M., Tramblay, Y., Reig, F., González-Hidalgo, J. C., Beguería, S., Brunetti, M., Kalin, K. C., Patalen, L., Kržič, A., Lionello, P., Lima, M. M., Trigo, R. M., El-Kenawy, A. M., Eddenjal, A., Türkes, M., Koutroulis, A., Manara, V., Maugeri, M., Badi, W., Mathbout, S., Bertalanič, R., Bocheva, L., Dabanli, I., Dumitrescu, A., Dubuisson, B., Sahabi-Abed, S., Abdulla, F., Fayad, A., Hodzic, S., Ivanov, M., Radevski, I., Peña-Angulo, D., Lorenzo-Lacruz, J., Domínguez-Castro, F., Gimeno-Sotelo, L., García-Herrera, R., Franquesa, M., Halifa-Marín, A., Adell-Michavila, M., Noguera, I., Barriopedro, D., Garrido-Perez, J. M., Azorin-Molina, C., Andres-Martin, M., Gimeno, L., Nieto, R., Llasat, M. C., Markonis, Y., Selmi, R., Ben Rached, S., Radovanović, S., Soubeyroux, J.-M., Ribes, A., Saidi, M. E., Bataineh, S., El Khalki, E. M., Robaa, S., Boucetta, A., Alsafadi, K., Mamassis, N., Mohammed, S., Fernández-Duque, B., Cheval, S., Moutia, S., Stevkov, A., Stevkova, S., Luna, M. Y., and Potopová, V.: High temporal variability not trend dominates Mediterranean precipitation, Nature, 639, 658–666, https://doi.org/10.1038/s41586-024-08576-6, 2025.

Viviroli, D., Dürr, H. H., Messerli, B., Meybeck, M., and Weingartner, R.: Mountains of the world, water towers for humanity: Typology, mapping, and global significance, Water Resour. Res., 43, https://doi.org/10.1029/2006WR005653, 2007.

Voudouri, K. A., Ntona, M. M., and Kazakis, N.: Snowfall Variation in Eastern Mediterranean Catchments, Remote Sensing, 15, 1596, https://doi.org/10.3390/rs15061596, 2023.

Wang, G., Che, T., Dai, L., Hu, Y., Wu, J., Meng, S., Kong, C., Wang, J., Feng, D., Wang, S., and Li, X.: Mapping snow cover frequency at 30 m for studying seasonal variations and topographic controls on the Tibetan Plateau, J. Hydrol., 660, 133303, https://doi.org/10.1016/j.jhydrol.2025.133303, 2025.

Wayand, N. E., Marsh, C. B., Shea, J. M., and Pomeroy, J. W.: Globally scalable alpine snow metrics, Remote Sens. Environ., 213, 61–72, https://doi.org/10.1016/j.rse.2018.05.012, 2018.

Ye, F., Cheng, Q., Hao, W., Yu, D., Ma, C., Liang, D., and Shen, H.: Reconstructing daily snow and ice albedo series for Greenland by coupling spatiotemporal and physics-informed models, International Journal of Applied Earth Observation and Geoinformation, 124, 103519, https://doi.org/10.1016/j.jag.2023.103519, 2023.

Zakeri, F. and Mariethoz, G.: Synthesizing long-term satellite imagery consistent with climate data: Application to daily snow cover, Remote Sensing of Environment, 300, 113877, https://doi.org/10.1016/j.rse.2023.113877, 2024.

Zhao, W., Fang, J., Yang, T., Lian, X., Winkler, A. J., Sun, F., and Gentine, P.: Observation-Constrained Physical Snow Water Equivalent Simulations Using a Physics-Guided Machine Learning Approach, Water Resources Research, 62, e2025WR041406, https://doi.org/10.1029/2025WR041406, 2026.

Zhong, L., Lei, H., and Gao, B.: Developing a Physics-Informed Deep Learning Model to Simulate Runoff Response to Climate Change in Alpine Catchments, Water Resources Research, 59, e2022WR034118, https://doi.org/10.1029/2022WR034118, 2023.